The Journal of
Undergraduate Research
in Physics

CONTENTS

Volume 18, Number 2
Spring, 2000

Produced by the Physics Department of Guilford College
for
The American Institute of Physics and the Society of Physics Students

THE JOURNAL OF UNDERGRADUATE RESEARCH IN PHYSICS

This journal is devoted to research work done by undergraduate students in physics and its related fields. It is a vehicle for the exchange of ideas and information by undergraduate students. Information for students wishing to submit manuscripts for possible inclusion in the Journal follows.

ELIGIBILITY
The author(s) must have performed all work reported in the paper as an undergraduate student(s). The subject matter of the paper is open to any area of pure or applied physics or physics related field.

SPONSORSHIP
Each paper must be sponsored by a full-time faculty member of the department in which the research was done. A letter from the sponsor, certifying that the work was done by the author as an undergraduate and that the sponsor is willing to be acknowledged at the end of the paper, must accompany the manuscript if it is to be considered for publication.

SUBMISSION
Two copies of the manuscript, the letter from the sponsor and a telephone number or E-Mail address where the author can be reached should be sent to:
Dr. Rexford E. Adelberger, Editor
THE JOURNAL OF UNDERGRADUATE RESEARCH IN PHYSICS
Physics Department
Guilford College
Greensboro, NC 27410

FORM
The manuscript should be typed, double spaced, on 8 1/2 x 11 inch sheets. Margins of about 1.5 inches should be left on the top, sides, and bottom of each page. Papers should be limited to fifteen pages of text in addition to an abstract (not to exceed 250 words) and appropriate drawings, pictures, and tables. Manuscripts may be submitted on a disk or as an E-mail attachment that can be read by a MacIntosh™. The files must be compatible with MicroSoft Word™ or PageMaker™.

ILLUSTRATIONS
Line drawings should be made with black ink on plain white paper. The line thickness should be sufficient to be reduced to column format. Each figure or table must be on a separate sheet. Photographs must have a high gloss finish. If the submission is on a disk, the illustrations should be in PICT, TIFF or EPS format.

CAPTIONS
A descriptive caption should be provided for each illustration or table, but it should not be part of the figure. The captions should be listed together at the end of the manuscript

EQUATIONS
Equations should appear on separate lines, and may be written in black ink. All equations should be numbered. We use EXPRESSIONIST™ to format equations in the Journal.

FOOTNOTES
Footnotes should be typed, double spaced and grouped together in sequence at the end of the manuscript.

PREPARING A MANUSCRIPT
A more detailed set of instructions and advice for authors wishing to prepare manuscripts for publication in the Journal of Undergraduate Research in Physics can be found in the back of each issue.

SUBSCRIPTION INFORMATION

The Journal is published twice each academic year, issue # 1 appearing in the fall and issue # 2 in the spring of the next calendar year. There are two issues per volume.

TYPE OF SUBSCRIBER	PRICE PER VOLUME
Individual	$US 5.00
Institution	$US 10.00

Foreign subscribers add $US 2.00 for surface postage, $US 10.00 for air freight.

Back issues may be purchased by sending $US 15.00 per volume to the editorial office.

To receive a subscription, send your name, address, and check made out to **The Journal of Undergraduate Research in Physics (JURP)** to the editorial office:

JURP
Physics Department
Guilford College
Greensboro, NC 27410

The Journal of Undergraduate Research in Physics is sent to each member of the Society of Physics Students as part of their annual dues.

DATA ANALYSIS FOR A LASER BASED DISPLACEMENT MONITORING SYSTEM OF A SILICON STRIP DETECTOR AT CERN

Gyöngyi L. Marian*
Kossuth Lajos University, Institute of Experimental Physics
Debrecen 4001, POB: 105, Hungary
and Institute for Nuclear Research of the Hungarian Academy of Sciences, Debrecen

Mark Behrens †
Department of Physics and Astronomy
University of Alabama
Tuscaloosa, AL 35487 USA
received March 29, 2000

ABSTRACT

The Silicon Microvertex Detector (SMD) is a subdetector of the L3 experiment at CERN. We determined the global and local displacements of the SMD sensors by analyzing data from the Laser Displacement Monitoring System.

INTRODUCTION

CERN, the European Center for Particle Physics, is located near Geneva, Switzerland. It is the largest particle physics research center in the world. In the Large Electron-Positron Collider (LEP), laboratory conditions very similar to the first few hundred billionths of a second of the beginning of the universe can be recreated. In the LEP, beams of electrons and positrons orbit in opposite directions in a 27 km circumference vacuum pipe buried in a tunnel 70 m under the surface. The beams, traveling near the speed of light, are guided by magnets to four collision points, where the L3, ALEPH, DELPHI and OPAL experiments are placed. Figure 1 shows L3, the largest detector. It has several subdetectors arranged in a layered structure: Silicon Microvertex Detector (SMD) [1]; Electromagnetic Shower Counter (BGO); Hadron Calorimeter and Muon Drift Chamber. The SMD subdetector is

Gyöngyi L. Marian graduated from the Kossuth University in Hungary. She is now a graduate student in the high energy physics group there and is a technical consultant for the Florida Institute of Technology.

Mark Behrens graduated from The University of Alabama. He is now a graduate student in mathematics at the University of Chicago.

Together, the performed the research described here at CERN (Switzerland), Kossuth University (Hungary) and the University of Alabama (USA).

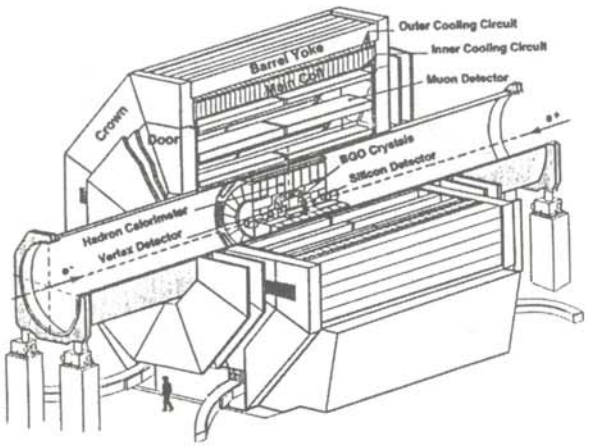

Figure 1
The L3 detector consists of 5 subdetectors: Silicon Microvertex Detector (SMD), Time Expansion Chamber (TEC), Electromagnetic Shower Counter (BGO), Hadron Calorimeter and the Muon Drift Chamber. The SMD is the closest to the beam pipe. It is capable of detecting short-lived particles such as the τ lepton .

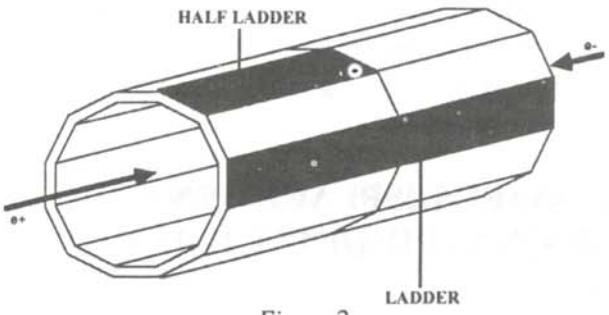

Figure 2

The geometry of the outer layer of the SMD. There are 12 double-sided silicon ladders (each of which has two separate half-ladders) mounted on the outer and on the inner wall of the SMD. The laser data analysis is performed taking in consideration only the data from the outer sensors of the SMD, since the laser spots illuminate only the outer half-ladders of this detector.

situated nearest to the beam pipe. It is designed to provide high precision position measurements near the interaction point. The measurements allow for reconstruction of the tracks to determine the decay point (the vertex) of short lived particles such as the τ lepton. The position of the SMD (as a rigid body) and its individual parts (sensors) might change due to thermal or other effects. Since the displacements can exceed the tracking precision, they must be monitored. The optical alignment monitoring system [2] (LDMS) identifies the location of the individual silicon sensors of the SMD with respect to the TEC to a precision on the order of 10 μm. The LDMS provides a continuous position measurement, tracking changes in the SMD geometry throughout the operational life of the detector. The LDMS was developed as a collaboration between the University of Alabama (USA) and the Kossuth Lajos University (Hungary) with contributions from the Central Research Institute for Particle Physics of the Hungarian Academy of Sciences (Hungary, the Technical University of Budapest (Hungary) and the Swiss Federal Institute of Technology (Switzerland). The present responsibility for the LDMS lies with the Florida Institute of Technology (USA) and Kossuth Lajos University (Hungary).

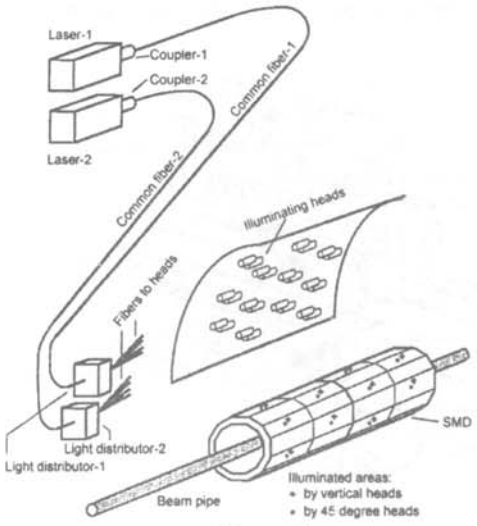

Figure 3

Schematic view of the optical laser displacement monitoring system (LDMS). Illuminating laser heads are mounted on the inner wall of the TEC (Time Expansion Chamber) which reflect the light on the surface of the SMD.

EXPERIMENTAL SETUP

The SMD is a microstrip semiconductor detector. It consists of two cylindrical layers of double sided silicon strip detectors. Each layer contains 12 silicon ladders, each of which consists of two separate half-ladders as shown in Figure 2. The latter are two electrically and mechanically joined double sided silicon sensors (wafers).

To describe the position of the pieces, a cylindrical coordinate system (r,ϕ,z) with the z axis pointing along the beam lines was chosen. On the outer side (the ϕ side) of the silicon wafer, there are strips (formed by doping the silicon and by lithographing aluminum contacts over the doped regions) that run parallel to the beam pipe intended to measure the (r- ϕ) coordinates. On the inner side (z side), the strips are perpendicular to the beam pipe and the outer strips. These strips are used when measuring the z coordinate. The readout pitch (the distance between one edge of one silicon strip to the same edge on the next silicon strip) of the SMD is 50 μm on the ϕ side and 200 μm on the z side (several strips are ganged on the z side).

The optical system of the LDMS (see Figure 3) has two IR (905 nm) laser diodes that are triggered every 10 seconds to produce 50 ns pulses. The light transmission system has two optical fibers of core diameter 400 μm transmitting the laser light to twenty four 50 μm core diameter fibers. These smaller diameter fibers transmit the light to optical heads, glued rigidly to the inner wall of the TEC. Each

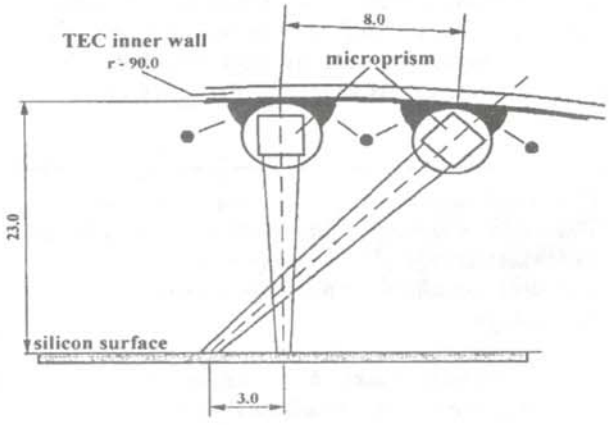

Figure 4

The optical laser heads reflect the light at 45° and 90° angles, allowing 3 measurements in r, r-ϕ, and z directions (the r is equivalent to the distance between the 45° and 90° laser spot positions)

head has a focusing lens and a prism that reflects the light at 45° and 90° onto the surface of the SMD as shown in Figure 4. There are 22 laser heads mounted one to a half-ladder, so there are a total 44 laser spots on the outer sensor layer. Each laser spot illuminates several neighboring readout strips. The laser light creates electron-hole pairs inside the semiconductor. Due to the electrical field applied between the two sides of this silicon sensor (junction - ϕ side and ohmic - z side), the charge carriers begin to drift and they are collected on the electrodes (strips). The electrical charge is collected from these by capacitors. At the end of each ladder, a complex read-out electronics converts the analog signals to digital format. The digitized signals are then sent to an optical receiver at the DAQ (data acquisition) "front-end" electronics. This optical receiver contains a receiver chip that converts the light signals back to electrical ones before passing them to the remainder of the DAQ.

A change in the measured centroid of the laser spots indicates relative rotational and/or translational motion between the SMD silicon sensors and the TEC. Translational movement parallel to the beam pipe is monitored on the z side; the rotation about the beam pipe is monitored on the outer ϕ side and the radial displacement from the interaction point is determined by observing the distance between the 45° and 90° spots.

ANALYSIS METHOD

The L3 event reconstruction program (REL3) is thousands of lines of FORTRAN code. It is a program that stages and reads data from tapes/disks and incorporates into its interpretation of the data important information about calibration, geometry of the detector and anything else necessary to prepare data for analysis. REL3 reads events one by one from the data storage and calls the Reconstruction User Analysis (RUANAL) subroutine. The user introduces analysis code in this subroutine.

The SMD events are retrieved from the L3 raw data stores.

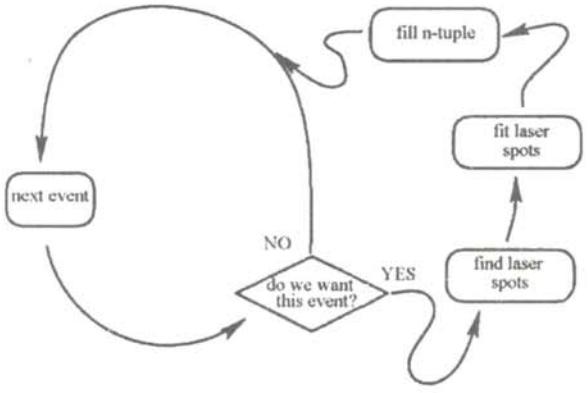

Figure 5

The event loop. The laser events are read out one by one and processed through an event loop.

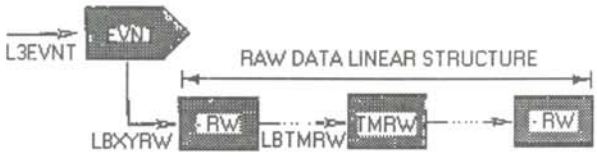

Figure 6

ZEBRA event structure. Beam Gate/laser events can be retrieved from zebra data banks using event pointers (LBEVNT, LBXYRW, LBTMRW etc.). The BG/laser bit, run number, date and time of event are in the EVNT event bank. The raw laser data can be retrieved from the TMRW data bank by following the raw linear structure the raw data banks.

The bulk of the analysis is performed at this stage. The laser spots are found and the shapes are fitted with Gaussian functions. The mean of the fitted signals, the centroid of the spot, is taken to be the positions of the laser spots. Time averages of individual positions are calculated. The reconstruction program produces an 'hbook' [4] file which contains 'n-tuples', documenting the laser spot positions with respect to time. These 'n-tuples' are like data tables, where the variables are the columns and each event is a row, that document the strip by strip ADC values (amplitude proportional to charge/strip) with respect to time. A set of histograms displaying the laser line shapes in the laser event is generated.

Getting an event

Inside hbook, the various data elements are stored as a ZEBRA data structure, one for each 'identifier'.[6] In fact, all identifiers (histogram or n-tuple numbers) are stored in an ordered array in a ZEBRA bank. Access to the information associated with the hbook data is via the reference link at the same offset as the identifier in the data part of the bank. Laser events (beam gate events) can be retrieved from ZEBRA data banks with calls to subroutines in the ZEBRA data manager package (ZEBRA MZ) . From the EVNT bank, we can retrieve the run number, date and time of the event. (see Figure 6). We also are able to look at the trigger word, in which we mainly are concerned with bit 13, the Beam Gate/laser trigger. We then follow the structural link to the XXRW->YYRW linear structure, in which all of the raw data may be found. In this linear structure, the TMRW bank in which the raw LDMS data are stored, is picked out.

Finding the spots

We developed a simple clustering algorithm to pick out the laser signal. The aim was to be quick, yet versatile enough to compensate for the lack of uniformity in the laser signals. Windows were defined on the appropriate half-ladders in which the laser signals were expected to appear from the design geometry. The ADC counts read in the strips within these windows were then scanned by a cluster finding algorithm to determine the existence and approximate location of the laser signal.

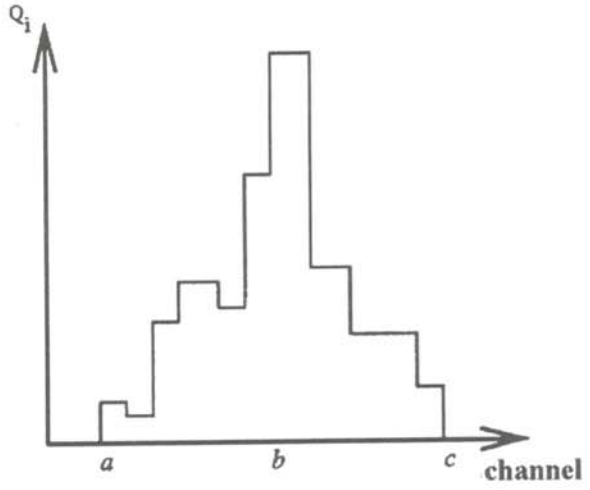

Figure 7
An example of the distribution of the charge produced by the laser light in the silicon sensor. a, b and c correspond to the first, last and maximum channel of the 'cluster'.

Cluster fitting
In LDMS data analysis, 'cluster' (see Figure 7) means groups of ADC signals. Having determined the existence of a cluster, the next step is to measure its position. We assume that:
° The charge Q_i read in the i^{th} channel of the cluster follows a normal distribution:

$$P(Q_i)dQ = \frac{1}{k\sqrt{2\pi < Q_i >}} \exp\left[-\frac{\left(Q - < Q_i >\right)^2}{2k^2 < Q_i >} \right] dQ, \qquad (1)$$

where k is a constant of proportionality with dimensions of the square root of charge and δQ_i proportional to the square root of the expectation value $<Q_i>$:

$$\delta Q_i = k\sqrt{<Q_i>}\,. \qquad (2)$$

° The charge distribution produced in the silicon by the laser itself follows a normal distribution.

Hence, we may fit the charge distribution with a Gaussian by minimizing:

$$\gamma^2(N, < x >, \sigma) = \sum_i^{\infty} \frac{\left[Q_i - N \exp \frac{\left(x_i - < x >\right)^2}{2\sigma_2^2} \right]^2}{k^2 Q_i}, \qquad (3)$$

where x_i is the spatial position of the i^{th} strip in the cluster, N, $<x>$ and σ are the normalization, mean and width of the fitted Gaussian and $<x>$ is the position of the laser spot. The associated error of $<x>$, $\delta<x>$, is obtained numerically from the principal radius of curvature of γ^2 (Equation 3) about its minimum in the <x> direction.

Time Averaging
The time average position is determined for each spot on an event by event basis. The laser spot position can be determined to a resolution of about 10 μm using Equation 3. The time average interval was chosen to be approximately 15 minutes, as movement due to temperature changes occurs over longer times. The time average, $<X>$ is found using a least squares method:

$$< X > = \frac{\sum_i \frac{< x_i >}{\left(\delta < x_i >\right)^2}}{\sum_i \frac{1}{\left(\delta < x_i >\right)^2}}, \qquad (4)$$

where the position values $<x_i>$ are weighted by the inverse square of their errors $\delta<x_i>$. The associated error $\delta<X>$ is given by:

$$\delta < X > = \frac{1}{\sqrt{\sum_i \frac{1}{\left(\delta < x_i >\right)^2}}}. \qquad (5)$$

RESULTS

The laser signal produced by one laser head at five different times of the year is presented in Figure 8. In Figure 9, the displacements are plotted versus time. The error bars represent statistical errors. The resolution of the z displacements is not as good as that of either the radial or tangential position due the readout pitch of the SMD is 150-200 μm on the z side as compared to 50 μm on the ϕ side. One can see the breaks in the data separating three L3 data taking periods. The gap around day 250 was caused by a crate power failure.

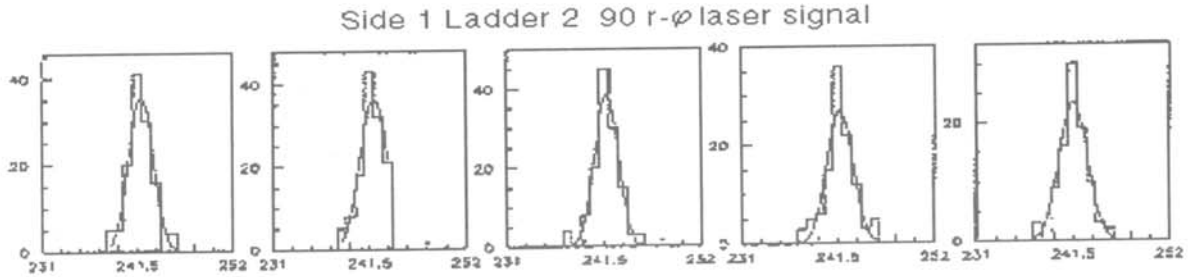

Figure 8
A fitted SMD signal from the same laser head over time.

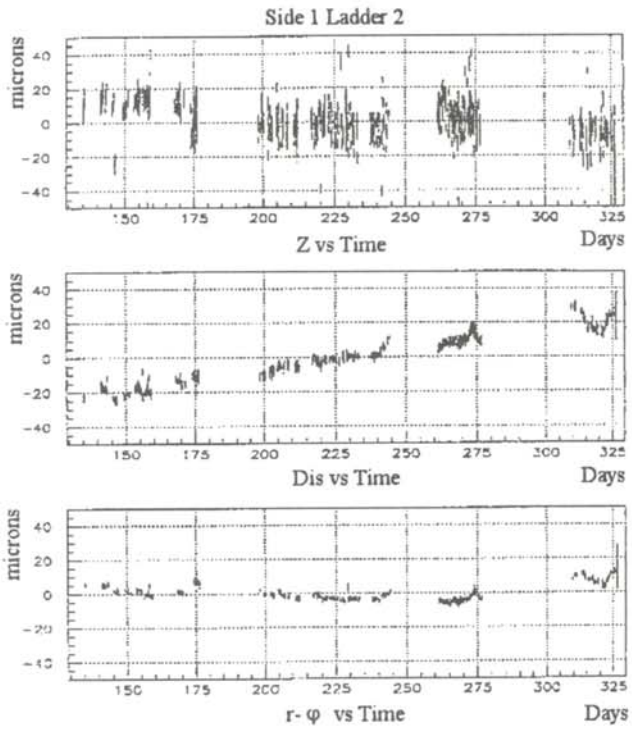

Figure 9
SMD movement parallel to the beam (z vs time); rotationally about the beam (r−ϕ vs time); and radially from the interaction point (Dis ≈ R vs time).

The time averaged plots are used to determine the movements of the half-ladders. In Figure 9, notice that the distance between the 90° and 45° spots is increasing. This indicates that one half-ladder has a steady radial movement of ≈ 40 μm towards the interaction point. In the r-ϕ direction, the rotational movement is ≈10 μm.

The displacements of all of the SMD half-ladders were compared. In the radial directions, a semi-local behavior isolated to a few half-ladders was observed. A small (≈10 μm) global displacement of the half-ladders was also observed.

LDMS is a sensitive and powerful monitor of the SMD displacement. It is sensitive to displacements on the order of a few microns. It is ultimately limited by the SMD's strip pitch, which is an order of magnitude greater. LDMS is able to resolve local as well as global SMD displacement trends. It has fulfilled, and in many respects exceeded, its design parameters.

ACKNOWLEDGMENTS

The authors wish to thank Professor Laszló Baksay for his help, guidance and support. This work was performed at the Kossuth Lajos University and the Institute for Nuclear Research of the Hungarian Academy of Sciences (Debrecen, Hungary) and at CERN. The project was supported in part by the Hungarian OTKA Fund No:TO17094 and T022238 and the US Department of Energy.

REFERENCES

* Current address of author: Department of Physics and Space Sciences, Florida Institute of Technology, 150 W. University Blvd., Melbourne, FL 32901. Magyongyi@aol.com
† Current address of author: Department of Mathematics, The University of Chicago, 5734S. University Avenue, Chicago, IL 60637.

1. M. Accari et.al., Nucl. Instr. and Meth in Phys. Res., "The L3 silicon Microvertex Detector", 3 June 1994.
2. "Optical Position Monitor System for the L3 Silicon Microvertex Detector", L3 TN No. 3, CERN, 22 March 1992.
3. "The L3 Experiment: Progress in Physics, Technology and International Collaboration", the L3 Administration and Communication Group, CERN, October 1988.
4. HBOOK (Statistical Analysis and Histogramming), CERNH-CN Program Library Long Writeup Y250, Geneva, Switzerland, September-May, 1995.
5. J. Swain and L. Taylor, "L3 Computing Guide", NUB-3065, CERN, Geneva, Switzerland, 1 May 1993.
6. "ZEBRA", CERN-CH Program Library Writeup Q100/ Q101, Geneva, Switzerland, February, 1995.

FACULTY SPONSOR

Professor Laszló Baksay, Head
Department of Physics and Space Sciences
Florida Institute of Technology
150 West University Boulevard
Melbourne, FL 32901
baksay@pss.fit.edu

MODELING PION FLOW IN A ^{139}La + ^{139}La COLLISION

Daniel Valente *
Department of Physics and Engineering
Hope College
Holland, MI 49423
received June 8, 2001

ABSTRACT

This study focused on the flow behavior of pions created in a ^{139}La + ^{139}La nuclear collision. The system was simulated and studied at beam energies of 400 MeV/A and 1200 MeV/A using the Boltzmann-Uehling-Uhlenbeck (BUU) transport model for nuclear collisions. The dependence of flow on centrality, the size of the impact parameter, was examined for both beam energies. The dependence of flow on the nuclear equation of state, as well as on Coulomb interactions, was studied. At 400 MeV/A, both positive and negative pions were found to exhibit flow for central (small) impact parameters and anti-flow for peripheral (large, on the size of the nuclear radius) impact parameters. Similar results were obtained at 1200 MeV/A, agreeing with previous experimental data. The predicted flow was insensitive to the choice of equation of state and the Coulomb interactions did not have any profound change on the pion behavior.

INTRODUCTION

When two nuclei collide, the interactions between them push nucleons away from the collision zone. Examining how particles flow away from this region provides information on the interactions experienced during the collision. In low-energy collisions, the short-range attractive component of the nuclear force causes the nuclei to rotate and be pulled around each other (Figure 1). In high-energy collisions, the nuclei scatter elastically due to the repulsive hard core of the nuclear force (Figure 1). With this knowledge, the nuclear interaction, or the nuclear equation of state (EoS), can be studied. The EoS is used to model interactions between particles. If we think of particles as being connected by springs, then in a stiff EoS, the particles would be connected by stiff springs; in a soft EoS, the particles would be connected by more flexible springs.

To gain information about the nuclear EoS from the trajectories of the particles involved in the collision, it is useful to define a physical quantity that describes how these particles are flowing away from the collision zone. In a collision, if forward moving particles (those traveling in the $+z$ direction) have a component of their momentum in the $+x$ direction (see Figure 1), then this is defined as *flow*. This is typically seen in the elastic scattering of high-energy collisions. In contrast, if the forward moving particles (those traveling in the $+z$ direction) have a component of their momentum in the $-x$ direction (see Figure 1), then this is defined as *anti-flow*. This is characteristic of low-energy collisions, where the particle interactions cause the nuclei to revolve around each other. Thus, on the average, systems with forward moving particles having an average momentum in the x direction, $\langle p_x \rangle$, that is positive exhibit *flow*, while systems with forward moving particles having a negative $\langle p_x \rangle$ exhibit *anti-flow*.

For particles moving backwards in the center-of-momentum (CM) frame, the opposite is true; backward moving particles having a positive $\langle p_x \rangle$ exhibit anti-flow, and backward moving particles having a negative $\langle p_x \rangle$ exhibit flow. The momenta of the particles in these directions also determine the strength of the flow—the greater the momenta, the greater the flow. To determine the directionality of the particle motion (forward or backward), the particle rapidity y is used:

$$y = \ln\left[\frac{E + p_z}{E - p_z}\right]. \quad (1)$$

Dan graduated from Hope College in May 2001 with a Bachelor of Science in Physics. This research was begun in the summer of his sophomore years as part of a NSF Research Experience for Undergraduates and was independently continued in his senior year. Dan is currently attending the graduate program in acoustics at the Pennsylvania Sate University, and is working towards his Ph.D. In his free time, Dan enjoys song writing, playing the guitar and drawing.

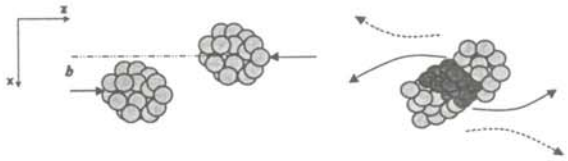

Figure 1

This figure shows the time progression of a nuclear collision. The two nuclei on the left side of the figure shows the system before the collision, where b *is the impact parameter of the collision. The right side of the figure shows the system after the collision. The darkly shaded region is the hot region where pions are produced. The solid lines represent the trajectories of single particles exhibiting anti-flow after the collision. The dotted lines represent the trajectories of single particles exhibiting flow after the collision. Note that the x-direction points towards the bottom of the page.*

One might expect that the velocity in the beam direction (v_z) would be used for this purpose, but rapidity is used in place of velocity for ease in transformations from the lab frame to the CM frame. Rapidity transforms linearly as:

$$y' = y_o + y_{frame}, \qquad (2)$$

instead of the complicated Einstein transformation needed for velocity. Together, both y and $\langle p_x \rangle$ give an informative description of the directionality of particle movement.

Typically, flow is examined on a plot of $\langle p_x \rangle$ versus y. The resulting graphs have a characteristic S-shaped curve to them, as seen in Figure 2. An inspection of the slope of the curve at the origin gives us a quantitative evaluation for flow. Forward moving particles with a positive $\langle p_x \rangle$ produce a positive slope about the origin, indicating flow. Forward moving particles with a negative $\langle p_x \rangle$ produce a negative slope, which is termed anti-flow. The steepness of the slope gives information on the amount of flow a system is exhibiting—the larger the slope, the greater the flow. A more extensive explanation of flow in nuclear reactions can be found in the literature. [1,2]

At high energies, nucleons in a collision always produce flow plots similar to Figure 2; they always exhibit flow. In energetic collisions, however, nucleons are not the only particles involved. Around the area of impact, a region of high-density nuclear matter is created. Conditions in this hot region are acceptable for the creation of a variety of particles. If the energy in the hot zone is above production threshold, a nucleon-nucleon collision can create a Δ particle. The Δ particle is a baryon with a lifetime of $\sim 10^{-23}$ *s* that decays into a nucleon by emission of a pion (pions are mesons consisting of a quark/anti-quark pair). A thorough discussion of meson production in nuclear collisions can be found elsewhere. [3]

A search of the literature found an experiment that examined an Au + Au system at 1.15 GeV, which was energetic enough to create Δ particles and pions. 4 It was found for this energy that pion flow is dependent upon impact parameter. For peripheral collisions (collisions in which the edges of the nuclei collide), positive pions and negative pions exhibit a flow that is in a direction opposite to that of the nucleons. This was attributed to shadowing and re-scattering effects of the spectator nucleons. Shadowing occurs when the residual nuclei block (shadow) the pions from reaching the detectors. Re-scattering occurs when the pions interact with the other particles involved in the collision and are scattered multiple times.

In this work, a computer model was used to simulate nuclear collisions, and the resulting flow behavior was examined. The goal of these simulations was to understand the experimental results. [4] Understanding why pions flow in a certain direction elucidates the properties of the hot zone and the interactions that pions experience in this region, thus providing vital information about the system.

THEORETICAL EXAMINATION OF THE ^{139}La + ^{139}La COLLISION: *BUU*

In this study, a ^{139}La + ^{139}La collision was modeled using the Boltzmann-Uehling-Uhlenbeck (BUU) transport model for nuclear collisions to examine pion flow. BUU simulated the collision of two nuclei by using Monte-Carlo techniques to track the trajectories of nucleons of the colliding nuclei as they move under the influence of a nuclear potential U. [5] The These nucleons have randomly generated initial positions constrained within a sphere the size of the nucleus and a randomly generated momentum

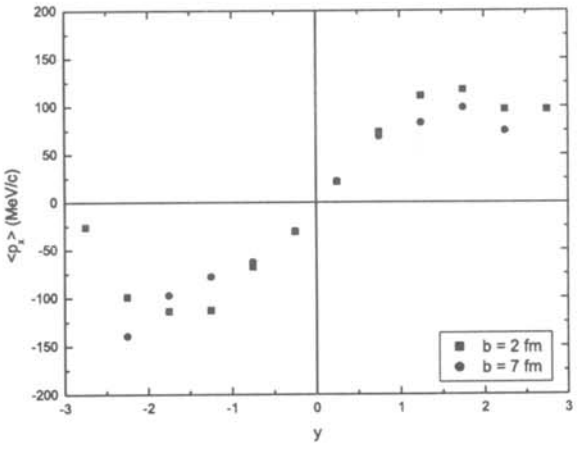

Figure 2

Typical flow curves for nucleons in 1200 MeV/A La + La collisions at impact parameters of 2 fm and 7 fm for a stiff EoS. The well defined S-curve is characteristic of flow plots.

constrained to be below the Fermi momentum for the ground state of the nucleus. At each time step, (the size of the time step is a parameter of the model), BUU solves a form of Newton's second law for every particle involved in the collision (including particles created in the collision), allowing their momenta and positions to be tracked as a function of time. The model takes into account the probabilities for particle-particle scattering using measured reaction cross sections, as well as the effects of the Pauli exclusion principle, forbidding collisions in which the final states of the scattered particles are occupied.

Since U describes the nuclear interaction, it inherently contains information about the nuclear equation of state. In effect, BUU tracks the change in the number of particles that have a certain momentum at a certain position from the original randomly generated sate to the final state caused by the interactions in the collision. An examination of this change yields information about the interactions described by the nuclear force (the EoS).

The energy of the collision and the impact parameter should have an effect on the flow of the particles. Since *flow* depends on the complex interactions experienced by the particles, perhaps the EoS can be probed by examining the *flow* behavior of pions in a collision. To test this, two separate impact parameters (central and peripheral) were examined at two beam energies (1200 MeV/A and 400 MeV/A) in a Lanthanum/Lanthanum system. A beam energy per nucleon (MeV/A) of 1200 MeV/A was run to compare to the experimental data [4]. A lower beam energy of 400 MeV/A was run to compare to the higher energy. Central collisions (those which are nearly head-on) were defined by an impact parameter of $b = 2$ fm. Peripheral collisions were defined as $b = 7$ fm, which is slightly larger than the radius of the Lanthanum nucleus.

The nuclear interaction is a parameter of the model as well, so two nuclear EoS, one stiff, momentum independent and one soft, momentum dependent, were examined to see if the definition of the EoS gave characteristic differences in *flow*. (In a momentum dependent EoS the trajectories of each particle are influenced by the momentum of the particles with which it interacts). Finally, to study the effects of the Coulomb interaction on *flow*, simulations were run with the effects of the Coulomb potential neglected. These simulations were also used to examine any differences between the *flow* behavior of positive and negative pions.

RESULTS

Figure 3 shows the results obtained for negative pions at 400 MeV/A for the stiff EoS. Here, a distinct difference can be seen in pion *flow* at different impact parameters. For the central ($b = 2$ fm) impact parameter, negative pions show signs of *flow* (positive slope about the origin), whereas in peripheral ($b = 7$ fm) impacts, the negative pions show signs of *anti-flow* (negative slope about the origin). The same is true for positive pions at the same energy.

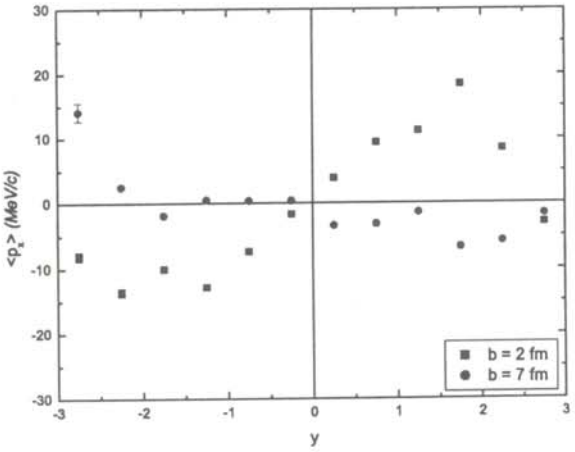

Figure 3
The flow curves for negative pions in 400 MeV/A La + La collisions at impact parameters of 2 fm and 7 fm for a stiff EoS. Here the impact parameter dependence is evident.

To gain insight on the impact parameter dependence, the development of *flow* over time is examined in Figure 4. In Figure 4, *flow* as a function of π^- emission time is plotted. Note that in Figure 4, unlike the *flow* plots, the y-axis is a weighted transverse momentum $\langle wp_x \rangle$ (MeV/c). Because of the symmetry of the collision, a particle with momentum p_x and rapidity y_1 going backward can be mapped to a particle with momentum $-p_x$ and rapidity $-y_1$. Thus, the weighting factor w is +1 for $y > 0$ and -1 for $y < 0$ so that the statistics in these calculations can be doubled. The x-axis is time in fm/c (~0.3 x 10^{-23} s). At both impact parameters, the pions emitted in early times of the collision exhibit *flow*. As the collision progresses, the peripheral collisions show a transition to *anti-flow*. The peak in *anti-flow* happens at a time of approximately 35 fm/c. A summary of all the *flow* results can be found in Table 1.

As can be seen in Table 1, both positive and negative pions behave similarly in all of the simulations. Because of the similarity, it is assumed that this *flow* behavior is a result of the geometry of the collision, rather than a Coulomb effect. A possible explanation for the peak in *anti-flow* for peripheral collisions follows directly from an investigation of Figure 4. When two nuclei collide in a central collision, the hot zone occurs in the middle of the large nucleonic mass that is subsequently formed. The pions created here have a difficult time escaping this central region, as they are re-absorbed by the residual nuclei. At all times in the collision, these pions are "carried" with the collection of nucleons and exhibit the same *flow* characteristics as the nucleons (Figure 5a). In peripheral collisions, however, the pions are not trapped in this large central region; they are created in a narrow neck region around the area of

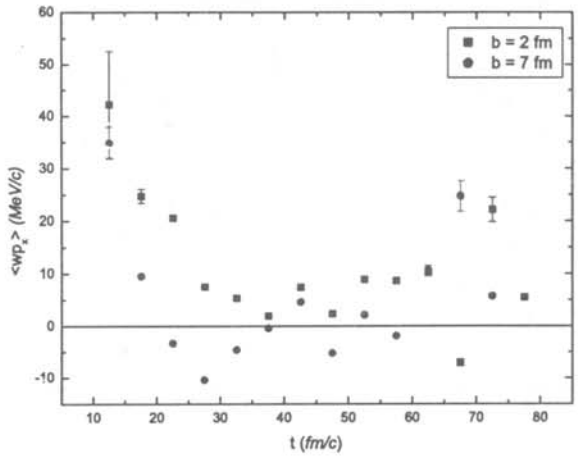

Figure 4

The time dependence of flow for negative pions in 400 MeV/A La + La collisions at impact parameters of 2 fm and 7 fm for a stiff EoS. This figure shows $<p_x>$ at the times the pions are emitted from the system. Integration of these curves over time yield Figure 3. At both impact parameters, the system shows flow at early times in the collision, but the peripheral show a transition to anti-flow at ~35 fm/c, suggesting a geometric effect.

impact. As the nuclei pass each other, the pions are forced in the direction of *flow*; any *anti-flow* path is blocked by the residual nuclei. However, when the nuclei begin to pass each other (at a time around 30-35 fm/c) the geometry of the collision shifts and the flow path is now blocked by the nuclei, thus causing the pions to exhibit *anti-flow* (see Figure 5b).

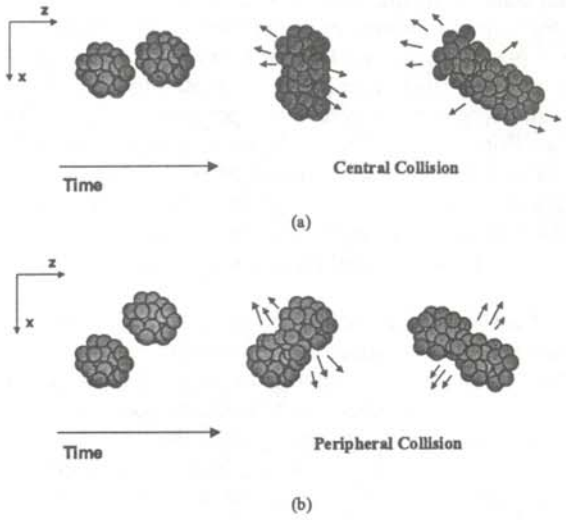

Figure 5

Pictorial representation describing the geometric effect suggested by Figure 3. The black arrows represent the paths of the pions. a) In central collisions, the pions are created in a region from which they have difficulty escaping. Therefore, they travel with the nucleons, exhibiting flow. b) In peripheral collisions the pions are created in a narrow neck region. The nucleons force flow at early times in the collision, but block this path at later times, forcing pion anti-flow.

At 1200 MeV/A with a stiff EoS, results similar to the lower energy data are obtained. As seen in Figure 6, the impact parameter dependence of *flow* is still apparent.

	Central Collisions (b = 2 fm)		Peripheral Collisions (b = 7 fm)	
	Stiff EoS	p dependent EoS	Stiff EoS	p dependent EoS
400 MeV/A				
Positive Pions	13.72	15.77	-3.561	*
Negative Pions	11.15	10.54	-1.381	*
Protons	115.9	101.5	86.20	110.3
Neutrons	100.1	90.56	76.28	96.68
1200 MeV/A				
Positive Pions	*	*	-17.54	-19.42
Negative Pions	5.720	4.465	-20.43	-16.94
Protons	94.51	93.17	89.46	96.38
Neutrons	85.04	84.97	89.30	98.98

*slope close to zero

Table 1

A summary of the flow results showing the slope of the fit line to the curve about the origin (the flow) for each simulation. The magnitude of the slope describes the degree to which particles are showing flow or anti-flow.

Central collisions exhibit *flow*, whereas peripheral collisions exhibit *anti-flow*. This is consistent with the experimental data. Figure 7 shows the *flow* as a function of time. These results for the higher energy differ slightly from those at the lower energy. At the high energy, less *flow* and a larger *anti-flow* are observed. Because the 1200 MeV/A collision is much more energetic, it happens on a much faster time scale. Therefore, the system never spends much time in a geometry that forces *flow*. Pions created in central collisions are still reabsorbed by the residual nuclei, but the pions created in peripheral collisions are emitted when the nuclei have nearly passed each other.

Because the pions are charged particles, Coulomb effects on the *flow* were examined in simulations that neglected Coulomb effects. When the data from these simulations were compared with the previous simulations, a small effect on *flow* due to the Coulomb interaction was found. For positive pions in central collisions, the Coulomb repulsion augments *flow*, since these pions are emitted with momentum that is already in the *flow* directions. In peripheral collisions, the geometry of the system causes the interaction to push the pions towards *anti-flow*. For negative pions at central collisions, the Coulomb interaction has the effect of adding to the *flow*, since these pions are attracted to the nucleons. For peripheral collisions, this attraction subtracts from *anti-flow*. In no case did the Coulomb interaction drastically change the *flow* or *anti-flow*, but it did slightly enhance it.

Lastly, no significant differences were found between the results for the stiff, momentum independent EoS (characteristic of the above simulations) and the soft, momentum dependent EoS. The *flow* characteristics of all particles were nearly the same (see Table 1).

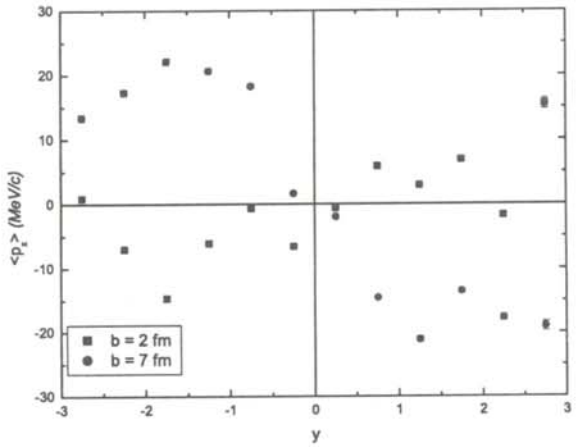

Figure 6
The flow curves for negative pions in 1200 MeV/A La + La collisions at impact parameters of 2 fm and 7 fm for a stiff EoS

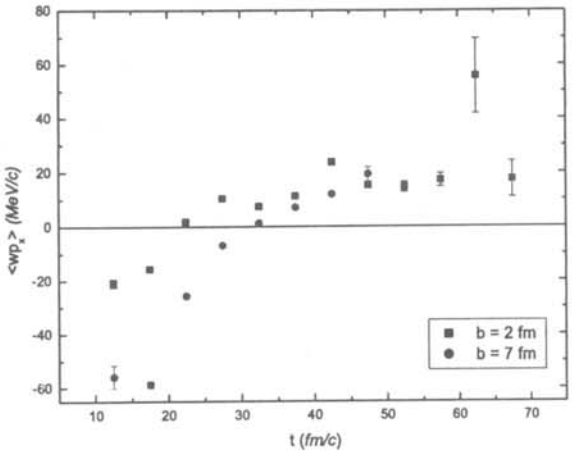

Figure 7
The time dependence of flow for negative pions in 1200 MeV/A La + La collisions at impact parameters of 2 fm and 7 fm for a stiff EoS

SUMMARY

The experimental evidence of the impact parameter dependence for *flow* has been confirmed by this study, however, it is apparent from the results in Table 1 that pion *flow* is not dependent on the nuclear EoS. It has been hypothesized that a geometric effect may be the cause of the impact parameter dependence, as well as the strength of the *flow*. This hypothesis has been supported by findings at two different beam energies. Further studies should focus on different parameters of the collision to confirm this geometric effect as well as investigations on what parameters can yield the most useful information about the equation of state.

ACKNOWLEDGMENTS

The author would like to thank Dr. Catherine Mader for her guidance, support, and advice during this research. Thanks also to the National Science Foundation for the REU grant PHY-9876955, without which this project would not have been possible. Finally, thanks to the Hope College Nuclear Group for all the useful insights and help with this project, especially the preliminary research done by Dana Burd.

REFERENCES

* 34004 W 14 Mile Road, West Bloomfield, MI, 48322.
1. S.D. Gupta and G.D Westfall, Physics Today, May 1993, pp. 34-40.
2. C.A. Ogilvie, W. Bauer, D.A. Cebra, J. Clayton, S. Howden, J. Karn, A. Nadasen, A. Vander Molen, G.D. Westfall, W.K. Wilson, and J.S. Winfield, Phys. Rev.

C42 (1990) R10.
3. K. S. Krane, Introductory Nuclear Physics, John Wiley & Sons, New York, (1988), pp. 653-692.
4. J.C. Kintner, et.al. Phys. Rev. Lett. 78, (1997) pp. 4165-4158.
5. W. Bauer, G. F. Bertsch, W. Cassing, and U. Mosel, Phys. Rev. C34, (1986) p. 2127.

FACULTY SPONSOR

Dr. Catherine M. Mader
Department of Physics and Engineering
Hope College
Holland, MI 49423
mader@physics.hope.edu

ENERGY STATES OF A GAUSSIAN WAVEPACKET IN AN INFINITE SQUARE WELL

David Etlinger *
Department of Physics and Astronomy
University of Rochester
Rochester, NY 14642
received April 20, 2001

ABSTRACT

An explicit expression is derived for the probability of an arbitrary energy state of a Gaussian wavepacket confined to an infinite square well potential. Approximations are made to determine the normalization factor and the probability. An upper bound on the errors due to the approximations is determined.

INTRODUCTION

Despite its simplicity and familiarity to most students of physics, the "square well" model of particle motion in quantum theory is still applicable in practice to new situations. [1,2] One of these arose recently in an explanation of spin flips in Bose-Einstein condensed atomic vapors confined in magnetic traps. [3]

One of the problems encountered in making simplified mathematical models of particle motion in confined spaces, such as traps, arises from the boundary conditions. For example, the infinite square well model requires a trapped particle to have a vanishing wave function outside the trap walls. However, the mathematical functions used to describe wave functions of particles moving in traps are frequently taken to be of Gaussian form, and the infinite wings of Gaussian functions are certainly non-zero outside the walls of the trap potential.

The Model

We will use a Gaussian wave packet to describe a particle moving in a one-dimensional square well. The wavefunction, as with all wavefunctions, must obey Schrödinger's equation:

David is currently a mathematics and physics major at the University of Rochester, and will obtain a minor in music as well. The research for this paper was conducted during his sophomore year as an independent project. After graduation, David plans to attend graduate school in mathematics or mathematical physics. His other interests include martial arts and playing piano, trumpet and guitar.

$$-\frac{\hbar^2}{2m}\frac{\partial^2\Psi(x,t)}{\partial x^2}+U(x)\,\Psi(x,t)=i\hbar\frac{\partial\Psi(x,t)}{\partial t}, \qquad (1)$$

where $U(x)$ is the potential well. At $t=0$, a Gaussian wave function of the form:

$$\Psi(x,0)=N\exp\left[-\frac{\left(x-\frac{L}{2}\right)^2}{2\alpha^2}\right]\exp\left[\frac{ipx}{\hbar}\right], \qquad (2)$$

is initially centered in the well, and evolves in time according to Equation 1.

The wavefunction can be rewritten entirely as a function of the distance from the center of the well:

$$\psi(x)\equiv\Psi(x,0)$$
$$=N\exp\left[-\frac{\left(x-\frac{L}{2}\right)^2}{2\alpha^2}\right]\exp\left[ik\left(x-\frac{L}{2}\right)\right]\exp\left[ik\frac{L}{2}\right], \qquad (3)$$

where for notational simplicity, the particle's wave number $k=p/\hbar$ is used in place of momentum p, $\psi(x)=\Psi(x,0)$, the parameter α governs the "size" of the Gaussian (roughly the width of the function at half-height), and N is the normalization constant. For convenience, we assume that k is positive (it is possible to modify our calculations for a negative momentum).

The model implicitly considers L to be the fixed length of the potential well. The values of x, α, and k are meaningful only in relation to this fixed value. To simplify later calculations, we rewrite the wavefunction in terms of three dimensionless variables:

$$\hat{x}\equiv\frac{x}{L}\quad\alpha\equiv\frac{\alpha}{L}\quad\hat{k}\equiv kL. \qquad (4)$$

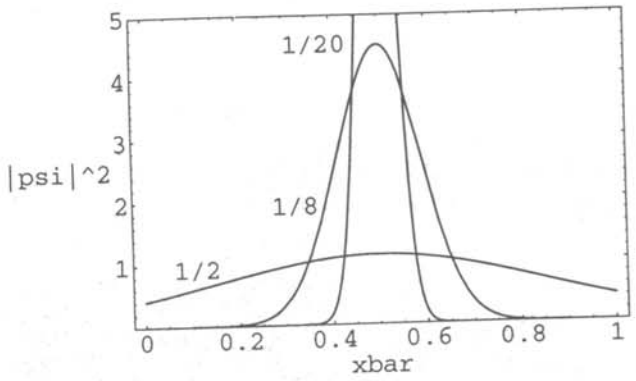

Figure 1
Plot of the probability density as a function of x for Gaussian wavepackets with α = 1/2, 1/8 and 1/20.

This allows Equation 3 to be rewritten as:

$$\psi(\tilde{x}) = N \exp\left[-\frac{\left(\tilde{x}-\frac{1}{2}\right)^2}{2\alpha^2}\right] \exp\left[ik\left(\tilde{x}-\frac{1}{2}\right)\right] \exp\left[\frac{ik}{2}\right], \quad (5)$$

where the well now extends from $\tilde{x}=0$ to $\tilde{x}=1$. Figure 1 shows the probability distribution, $|\psi(\tilde{x})|^2$, for several values of α. The shapes are the "packets". Wider packets have larger values of α. Note that the momentum term does not affect the packet shapes shown in Figure 1.

Energy and momentum are quantized in a traditional square well due to boundary conditions:

$$k_n = \frac{n\pi}{L}, \; E_n = \frac{\hbar^2}{2m} k_n^2 . \quad (6)$$

In the dimensionless notation, the momentum is:

$$\overline{k}_n = n\pi . \quad (7)$$

The primary challenge is to obtain a simple predictive understanding from the probability distribution of the energies that are possible for the particle. That is, to predict reliably, by reference only to the two packet parameters k and α, the most probable particle energies. The answer is not likely to be the result given in Equation 6 because of the Heisenberg Uncertainty Principle. The spatial confinement of the Gaussian function, roughly within the range $|\tilde{x} - 1/2| \le \alpha$, implies the presence of "uncertainty momenta" due to the confinement of the packet in the well, independent of the value of k.

The role of α deserves further discussion. It does not just control the width of the packet. Rather, it serves as a kind of "wave-particle selector". The larger the value of α, the less spatially localized the packet, and the more the behaves like a wave. Consequently, higher values of α imply (due to the Uncertainty Principle) that the packet will have a smaller variance (i.e., less energy variability).

Any Gaussian wave function has non-zero value outside the walls of the square well. This leads to an approximation in obtaining our energy estimates, and thus, to the need to establish bounds on the error introduced by the approximations. Gaussian wave packets are sometimes used in textbook discussions of particle behavior, but elementary texts don't generally carry through either an estimate or a careful bound of the errors introduced. Before we can actually calculate an expression for the energy probabilities, we need to solve for the normalization constant. In doing so, we will also do the bulk of the work required to bound the errors.

Normalization and Error Bounding

The factor N in Equation 3 is the normalization constant. To solve for it, we use the fact that the sum of the probabilities for all locations is 1:

$$\int_0^1 \left| N \exp\left[-\frac{\left(\tilde{x}-\frac{1}{2}\right)^2}{2\alpha^2}\right] \exp\left[ik\left(\tilde{x}-\frac{1}{2}\right)\right] \exp\left[\frac{ik}{2}\right] \right|^2 d\tilde{x} = 1. \quad (8)$$

After we eliminate the factors with absolute magnitude equal to unity (recall that $|e^{i\phi}| = 1$, for any real ϕ), this simplifies to:

$$N^2 \int_0^1 \exp\left[\frac{-(\tilde{x}-1/2)^2}{\alpha^2}\right] d\tilde{x} = 1 . \quad (9)$$

With these limits of integration, the integral in Equation 9 cannot be carried out analytically. However, we can evaluate the integral if the limits are different:

$$N^2 \int_{-\infty}^{+\infty} \exp\left[\frac{-(\tilde{x}-1/2)^2}{\alpha^2}\right] d\tilde{x} = 1 . \quad (10)$$

The integral in Equation 10 can be found in most integral tables [4], giving a value of N:

$$N = \frac{1}{\sqrt{\alpha}\sqrt{\pi}} . \quad (11)$$

Unfortunately, the integral in Equation 10 includes the contribution of the wavefunction outside of the potential well. Because of the infinite height of the potential wall, the contribution due to the wave function outside the potential well should be discarded. Instead of discarding it, we include it and show under what conditions the error introduced is so small that it can be tolerated. The bound that is establish for the error tells under what parameter conditions the model is physically reliable.

To determine the bound of the error, the integral in Equation 9 is separated into two parts. The first part is the approximation; the second part is the error. We will find the upper bound for this integral:

$$\int_0^1 |\psi(\bar{x})|^2 d\bar{x} \equiv \int_{-\infty}^{+\infty} |\psi(\bar{x})|^2 d\bar{x} - \int_{-\infty}^{0} |\psi(\bar{x})|^2 d\bar{x} - \int_1^{+\infty} |\psi(\bar{x})|^2 d\bar{x}$$
$$\equiv \int_{-\infty}^{+\infty} |\psi(\bar{x})|^2 d\bar{x} - 2\int_1^{+\infty} |\psi(\bar{x})|^2 d\bar{x}$$
$$\equiv \int_{-\infty}^{+\infty} |\psi(\bar{x})|^2 d\bar{x} - E_{norm}, \quad (12)$$

where E_{norm} is the size of the error. The equivalences in Equation 12 are valid for our wave packet, but not necessarily for all wavefunctions.

From Equations 9 and 12:

$$E_{norm} = 2\int_1^{\infty} |\psi(\bar{x})|^2 d\bar{x} = \int_1^{\infty} \exp\left[\frac{-(\bar{x}-1/2)^2}{\alpha^2}\right] d\bar{x}. \quad (13)$$

To simplify the integral in Equation 12, we make the substitution, $z = 2\bar{x} - 1$:

$$E_{norm} = 2\int_1^{\infty} \exp\left[\frac{-(\bar{x}-1/2)^2}{\alpha^2}\right] d\bar{x} = \int_1^{\infty} \exp\left[\frac{-z^2}{4\alpha^2}\right] dz. \quad (14)$$

Since $z \geq 1$ over the entire range of integration, $z^2 \geq z$. Therefore, Equation 14 can be rewritten to give the upper bound of the error as:

$$E_{norm} \leq \int_1^{\infty} \exp\left[\frac{-z}{4\alpha^2}\right] dz = 4\alpha^2 \exp\left[\frac{-1}{4\alpha^2}\right]. \quad (15)$$

Figure 2 shows the upper bound of the error as a function of α. The normalization integral, Equation 9, must equal 1. Therefore, we confine our attention to the range of values of α where the upper bound of $E_{norm} << 1$. For the sake of concreteness, we will assume that $\alpha < 1/8$, or $E_{norm} \leq 7 \times 10^{-9}$ (this might seem needlessly small, but it will keep later error bounds manageable). Figure 1 shows the packet for $\alpha = 1/8$.

Calculation of Energy Probabilities

Background

For a "square well" potential, one for which $U(x)$ between two infinite potential walls at $x = 0$ and $x = L$ (which we write as $\bar{x} = 0$ and $\bar{x} = 1$, the wavefunction of the n^{th} energy eigenstate is:

$$\Psi_n(\bar{x},t) = \exp\left[-\frac{iE_n t}{\hbar}\right]\sqrt{2}\sin(n\pi\bar{x}) = \exp\left[-\frac{iE_n t}{\hbar}\right]\psi_n(\bar{x}). \quad (16)$$

The superposition principle states that any linear superposition of valid wave functions is also a valid wave function. The most general solution to Schrödinger's equation is an infinite sum of the stationary states:

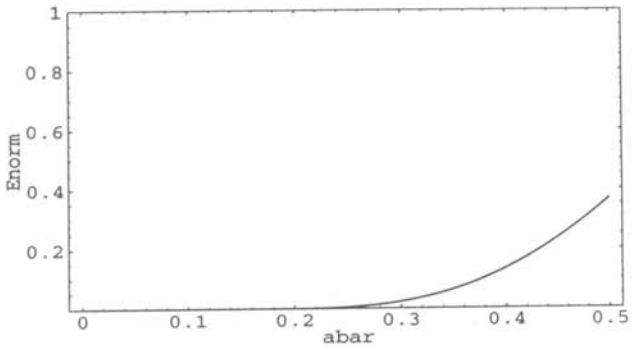

Figure 2

The size of the error in the normalization of the approximation to the Gaussian wave packet as a function of α, the width of the packet.

$$\Psi(\bar{x},t) = \sum_{n=1}^{\infty} c_n \Psi_n(\bar{x},t) = \sum_{n=1}^{\infty} c_n \exp\left[-\frac{iE_n t}{\hbar}\right]\psi_n(\bar{x}). \quad (17)$$

Each term in the sum corresponding to a specific particle energy E_n. A particle whose wavefunction is given by the sum in Equation 17 will have a probability of being found in the n^{th} energy state given by:

$$p_n = |c_n|^2. \quad (18)$$

To find values for c_n, note that the functions $\psi_n(\bar{x}) = \sqrt{2}\sin(n\pi\bar{x})$ are orthogonal, so:

$$\int_0^1 \psi_m^*(\bar{x})\,\psi_n(\bar{x})\,d\bar{x} = \delta_{mn}, \quad (19)$$

where δ_{nm} is called the Kronecker delta and is defined as:

$$\delta_{mn} = 0 \;\; m \neq n \;\; ; \delta_{mn} = 1 \;\; m = n. \quad (20)$$

Now consider the general solution to the Schrödinger equation at time *t=0:*

$$\Psi(\bar{x},0) = \sum_{n=1}^{\infty} c_n \psi_n(\bar{x}). \quad (21)$$

Note that the time exponential has dropped out. Now multiply both sides of this equation by $\psi_m(\bar{x})$ and integrate. The Kronecker delta will cause all the terms to cancel except for the case $n = m$:

$$\int_0^1 \psi_m^*(\bar{x})\Psi(\bar{x},0)\,d\bar{x} = \sum_{n=1}^{\infty} c_n \int_0^1 \psi_m^*(\bar{x})\,\psi_n(\bar{x})\,d\bar{x}$$
$$= \sum_{n=1}^{\infty} c_n \delta_{mn} = c_m. \quad (22)$$

Now, we calculate the values of the c_n's to predict the range of energies that will be present when $\Psi(\bar{x},0)$ is given by the Gaussian function in Equation 5.

The Gaussian Packet

Now to solve for the c_n's in the case of the Gaussian wave packet. The integral in Equation 22 is challenging because it cannot be evaluated exactly; approximate techniques will be needed to find the probability of finding the system in the n^{th} energy state. To find the c_n's, we use a technique similar to that used to find the normalization constants. The first approximation is to assume that the limits of the

integral go from -∞ to +∞, rather than from 0 to 1. Then we find the upper bound of the error for this approximation.

$$\begin{aligned} c_n &= \int_0^1 \psi(\bar{x})\,\psi_n(\bar{x})\,d\bar{x} \equiv \int_{-\infty}^{\infty} \psi(\bar{x})\,\psi_n(\bar{x})\,d\bar{x} \\ &- \int_{-\infty}^{0} \psi(\bar{x})\,\psi_n(\bar{x})\,d\bar{x} - \int_1^{\infty} \psi(\bar{x})\,\psi_n(\bar{x})\,d\bar{x} \\ &\equiv \int_{-\infty}^{\infty} \psi(\bar{x})\,\psi_n(\bar{x})\,d\bar{x} - 2\int_1^{\infty} \psi(\bar{x})\,\psi_n(\bar{x})\,d\bar{x} \\ &\equiv \int_{-\infty}^{\infty} \psi(\bar{x})\,\psi_n(\bar{x})\,d\bar{x} - E_{tot}\,, \end{aligned} \tag{23}$$

where E_{tot} is the error in the approximation.

To find an analytic expression for the integral in the last part of Equation 23, we make the substitution $y = \bar{x} - 1/2$ giving:

$$\psi_n(y) = \sqrt{2}\,\sin\left[n\pi\left(y + 1/2\right)\right]. \tag{24}$$

Using the expression from equation 5 for the Gaussian packet:

$$c_n = \Delta\int_{-\infty}^{\infty} \exp\left[-\frac{y^2}{2\alpha^2}\right]\exp\left[i\dot{k}y\right]\sin\left[n\pi\left(y + 1/2\right)\right]dy, \tag{25}$$

where Δ is the constant factor:

$$\Delta = \sqrt{\frac{2}{\alpha\sqrt{\pi}}}\,\exp\left[\frac{i\dot{k}}{2}\right]. \tag{26}$$

Using Euler's theorem to replace the sine term with two exponentials gives:

$$\begin{aligned} c_n &= \frac{\Delta}{2i}\int_{-\infty}^{\infty} \exp\left[-\frac{y^2}{2\alpha^2}\right]\exp\left[i\dot{k}y\right]\exp\left[in\pi\left(y + 1/2\right)\right]dy \\ &- \frac{\Delta}{2i}\int_{-\infty}^{\infty} \exp\left[-\frac{y^2}{2\alpha^2}\right]\exp\left[i\dot{k}y\right]\exp\left[-in\pi\left(y + 1/2\right)\right]dy. \end{aligned} \tag{27}$$

Combining like powers of n gives:

$$\begin{aligned} c_n &= \frac{\Delta}{2i}\exp\left[\frac{in\pi}{2}\right]\int_{-\infty}^{\infty} \exp\left[-\frac{y^2}{2\alpha^2}\right]\exp\left[iy\left(\dot{k} + n\pi\right)\right]dy \\ &- \frac{\Delta}{2i}\exp\left[\frac{-in\pi}{2}\right]\int_{-\infty}^{\infty} \exp\left[-\frac{y^2}{2\alpha^2}\right]\exp\left[iy\left(\dot{k} - n\pi\right)\right]dy. \end{aligned} \tag{28}$$

Equation 28 has an analytical solution that can be determined by using the general form found in many integral tables: [4]

$$\int_{-\infty}^{\infty} \exp\left(-au^2\right)\exp\left(ibu\right)du = \sqrt{\frac{\pi}{a}}\,\exp\left(-\frac{b^2}{4a}\right). \tag{29}$$

Using Equation 29 and rearranging some terms, the integrals in Equation 28 yield:

$$\begin{aligned} c_n &= \sqrt{\frac{\pi}{2}}\,i\Delta\alpha\exp\left(\frac{in\pi}{2}\right) \\ &\times\left\{\exp\left(-in\pi\right)\exp\left[-\frac{\alpha^2(n\pi-\dot{k})^2}{2}\right] - \exp\left[-\frac{\alpha^2(n\pi+\dot{k})^2}{2}\right]\right\}. \end{aligned} \tag{30}$$

Since $\exp(in\pi) = (-1)^n$, and using Equation 26, we can write Equation 30 as:

$$\begin{aligned} c_n &= i\sqrt{\alpha\sqrt{\pi}}\,\exp\left(\frac{i\dot{k}}{2}\right)\exp\left(\frac{in\pi}{2}\right) \\ &\times\left\{(-1)^n\exp\left[-\frac{\alpha^2(n\pi-\dot{k})^2}{2}\right] - \exp\left[-\frac{\alpha^2(n\pi+\dot{k})^2}{2}\right]\right\}. \end{aligned} \tag{31}$$

The approximate value of the probability of finding Gaussian packet in the n^{th} energy state becomes:

$$\begin{aligned} p_n &= \left|c_n\right|^2 \\ &= \alpha\sqrt{\pi}\left\{(-1)^n\exp\left[-\frac{\alpha^2(n\pi-\dot{k})^2}{2}\right] - \exp\left[-\frac{\alpha^2(n\pi+\dot{k})^2}{2}\right]\right\}^2. \end{aligned} \tag{32}$$

In anticipation of the analysis of the results, we define:

$$k_\alpha = \frac{1}{\alpha}\,. \tag{33}$$

This change will make the interpretation of the results slightly easier. By convention, α is used when discussing the original packet and k_α is used when discussing the energy distributions. Making the substitution in Equation 33 into Equation 32 gives:

$$p_n = \frac{\sqrt{\pi}}{k_\alpha}\left\{(-1)^n\exp\left[-\frac{(n\pi-\dot{k})^2}{2k_\alpha^2}\right] - \exp\left[-\frac{(n\pi+\dot{k})^2}{2k_\alpha^2}\right]\right\}, \tag{34}$$

Figure 3 shows p_n as a function of n for two different sets of parameters: one with $\dot{k} = 0$ and a relatively large value of k_a; and one for $\dot{k} = 30\,\pi$ and small k_a. Figure 3 is jagged because p_n is only defined for the integer values of n. We have interpolated a continuous curve to add visual clarity. When $\dot{k} = 0$, p_n is exactly 0 for even values of n.

Upper Bound of Error

We now find the upper bound to the error, E_{tot}, given in Equation 23. Using the same technique as done in the calculation of the upper bound to the error in the normalization constant, E_{norm}, (Equations 9 - 15). From Equation 23:

$$E_{tot} = 2\int_1^\infty \psi(\tilde{x})\,\psi_n(\tilde{x})\,d\tilde{x} = 2\sqrt{2}\int_1^\infty \psi(\tilde{x})\sin(n\pi\tilde{x})\,d\tilde{x}$$
$$\le 2\sqrt{2}\int_1^\infty \psi(\tilde{x})\,d\tilde{x} \le 2\sqrt{2}\int_1^\infty \left|\psi(\tilde{x})\right| d\tilde{x}$$
$$\le 2\sqrt{2}\int_1^\infty \exp\left[-\frac{(\tilde{x}-1/2)^2}{2\alpha^2}\right] d\tilde{x}. \qquad (35)$$

Evaluating the integral in Equation 35 gives:

$$E_{tot} \le 8\sqrt{2}\,\alpha^2 \exp\left[-\frac{1}{8\alpha^2}\right]. \qquad (36)$$

To decide how large is upper bound is, we compare it to the absolute value of c_n, since we are only interested in the magnitude of the error:

$$\frac{E_{tot}}{|c_n|} \le \frac{8\sqrt{2\,\alpha^3}}{\sqrt[4]{\pi}} \exp\left[-\frac{1}{8\alpha^2}\right] \exp\left[\frac{\alpha^2(n\pi-\tilde{k})^2}{2}\right]. \qquad (37)$$

Using Equation 37, the error can be made less than any desired percentage of the approximation, by choosing a small enough value of α.

Figure 4 shows the upper bound of the error, E_{tot}, from Equation 36 for α =1/8, plotted as a function of the distance $|n\pi-\tilde{k}|$.

Analysis of Results

The expressions we have derived for c_n (Equation 34) and p_n (Equation 36) can be written in a simpler form. The ratio of the two exponentials in Equation 34 is:

$$\text{ratio} = \frac{\exp\left[-\frac{\alpha^2(n\pi+\tilde{k})^2}{2}\right]}{\exp\left[-\frac{\alpha^2(n\pi-\tilde{k})^2}{2}\right]} = \exp\left[-\frac{2\tilde{k}n\pi}{k_\alpha^{\,2}}\right]. \qquad (38)$$

The numerator in Equation 38 will become negligible compared to the denominator, provided $\tilde{k}$ is sufficiently

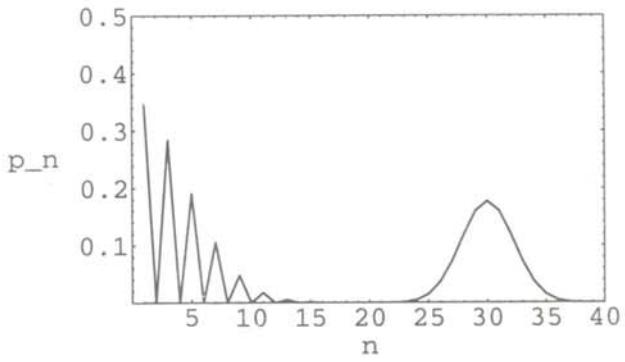

Figure 3
The probability of finding the Gaussian packet in energy state n vs n for: ($\tilde{k}$ = 0, k_a = 20) and ($\tilde{k}$ = 30π, k_a = 10).

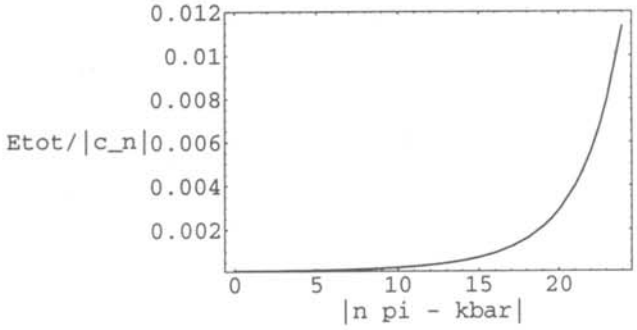

Figure 4
Ratio of the error in the coefficient to the size of the coefficient for the Gaussian wave packet as a function of $|n\pi-\tilde{k}|$ for α = 1/8.

large compared to $k_\alpha^{\,2}$. To keep the error bound small, $k_\alpha^{\,2}$ is large because α is a small number. For example, if k_a = 10 and $\tilde{k}$ = 10π, then at n = 1, the ratio (in Equation 39) ≈ 0.14. Larger values of n will only decrease this ratio, the exponential form ensuring that the ratio rapidly approaches zero. Therefore, if we impose an additional constraint on our parameters: that $\tilde{k} \ge k_\alpha^2/\pi$, we can ignore the top exponential. This allows us to rewrite Equation 34 in a much simpler form:

$$c_n \approx (-1)^n\, i\sqrt{\frac{\sqrt{\pi}}{k_\alpha}} \exp\left(\frac{i\tilde{k}}{2}\right) \exp\left(\frac{in\pi}{2}\right) \exp\left[-\frac{(n\pi-\tilde{k})^2}{2k_\alpha^{\,2}}\right]. \qquad (39)$$

Equation 36 can be approximated as:

$$p_n \approx \frac{\sqrt{\pi}}{k_\alpha} \exp\left[-\frac{(n\pi-\tilde{k})^2}{k_\alpha^{\,2}}\right]. \qquad (40)$$

Equation 40 is a Gaussian distribution, as is made obvious by our k_α notation. This packet is in some sense the complement to the Gaussian packet with which began. It is centered at $n = \tilde{k}/\pi$, and its width is controlled by k_α (note the lack of the 1/2-factor in the exponent). The effect of requiring a large $\tilde{k}$ is now evident: it ensures that the probability distribution is essentially Gaussian, and that one energy level can be considered the "primary" energy level. By the Uncertainty Principle, as the position wavepacket becomes narrower, the range of possible energies becomes broader, and vice versa. This is confirmed by the form of these two packets and the inverse relation between $\tilde{k}$ and k_α.

We can conclude that the range of likely energy levels for the particle is roughly:

$$n = \frac{\tilde{k}}{\pi} \pm \frac{k_\alpha}{4}. \qquad (41)$$

The upper bound for the error in the probability (see Figure 4) is tolerable in this range as well. For $|n\pi-\tilde{k}|$=24, or n=$\tilde{k}/\pi \pm 3k_\alpha$, the error is 1.1%.

Summary

We began with a Gaussian wave function, Equation 5, in an infinite square well potential. The goal of the analysis was to predict the likely energies for the system. The first task was to normalize the wavefunction. In doing so, we made approximations and exhibited an upper bound to the error in the normalization constant, Equation 15 . This also established the range of parameters for which our model is physically meaningful.

We then used the theory of orthogonal functions and the superposition principle to show how to express any wavefunction as an infinite sum, and to calculate the coefficients of the terms of that sum, Equation 22. The absolute square of a particular coefficient gives the probability of the corresponding energy level. We then applied the general expression to our specific wavefunction. This again required approximations. The upper bound on the error in the approximation was once again determined.

Finally, we imposed the additional condition that k be large enough so that we could approximate our expression for the probability that the system be in the n^{th} energy state, p_n , as another Gaussian. This allowed us to derive a very simple expression for the most likely energy levels of the system, Equation 41.

References

* current address of the author: CPU 274418, University of Rochester, Rochester, NY 14627-4418 de001i@mail.rochester.edu.

1. Ohanian, Hans C., Modern Physics 2nd Ed. New Jersey: Prentice Hall, 1995
2. Griffiths, David J., Introduction to Quantum Mechanics, New Jersey: Prentice Hall, (1995).
3. Q-H. Park and J.H. Eberly, Phys. Rev. Lett., 85, (2000), p. 4195.
4. Spiegel, Murray R., Mathematical Handbook, New York: McGraw-Hill, (1968).

Faculty Sponsor

Dr. J. H. Eberly
Director, Rochester Theory Center for Optical Sciences and engineering
Andrew Carnegie Professor of Physics and Professor of Optics
Department of Physics and Astronomy
University of Rochester
Rochester, New York 14627
Eberly@pas.rochester.edu

LABORATORY MEASUREMENTS OF VELOCITY PROFILES IN SIMULATED TORNADO-LIKE VORTICES

J. David Cleland *
Department of Physics
Miami University
Oxford, OH 45056
received January 10, 2001

ABSTRACT

Axial vertical velocity measurements of simulated super-critical tornado-like vortices were made in the Miami University Tornado Vortex Chamber (TVC). Improvements to the Miami TVC tornado generation mechanisms and data acquisition methods aided in the attainment of data with spatial resolution never before achieved in the study of simulated vortices. Axial vertical velocity measurements are presented as a function of super-critical vortex height for varying swirl ratio, and are referred to as velocity profiles. The data suggest a strong correlation between super-critical inner core region diameter and swirl ratio, as well as an apparent breakdown of super-critical structure well below vortex breakdown (vortex bubbling).

INTRODUCTION

In the last twenty-five years, several research teams and individuals have had notable success in simulating tornado-like vortex flows in the laboratory[1] . Figure 1 shows a photo of a simulated vortex in the Miami Tornado Vortex Chamber. (TVC). The laboratory environment provides a degree of experimental precision, control and repeatability for making measurements on vortices that is nearly impossible in nature. The atmospheric factors that are involved in creating an actual tornado in a thunderstorm environment (dynamic, thermodynamic and microphysical) are usually simplified or omitted in a laboratory simulation. Despite this, the utilization of laboratory generated vortices is a powerful tool in understanding the dynamics of a tornado.

Obtaining accurate data for vertical velocities along the height of a tornado's rotational axis, the axial vertical velocity, has had a history of eluding interested researchers, both in and out of the laboratory. Methods have been proposed to measure pressure deficits in actual tornado core regions. However, none of these ideas have been realized nor have met with success. Scientists in the

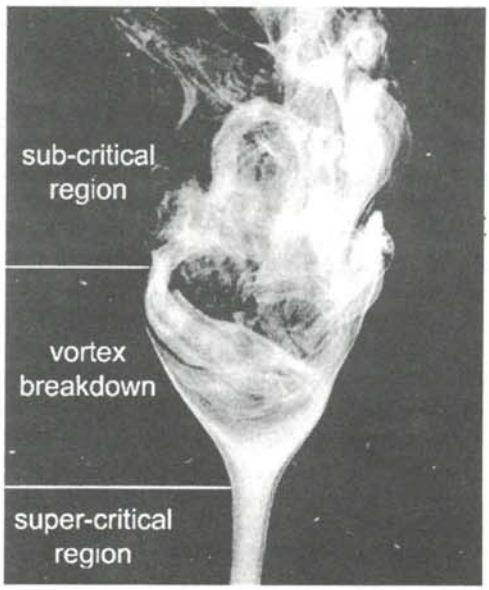

Figure 1
Photograph of a simulated vortex in the Miami TVC. Tornado-like vortices display three distinct dynamic regions: a tightly structured super-critical region; the vortex breakdown bubble; the turbulent sub-critical region.

David graduated in December 2000 with a degree in engineering. His research began in the fall of his junior year, and culminated with an Undergraduate Summer Scholars grant in the summer of 2000. David currently works as an electrical engineer in Chicago, IL, and plans to attend graduate school in applied physics in the fall of 2002. He spends most of his free time playing music or designing high fidelity audio systems.

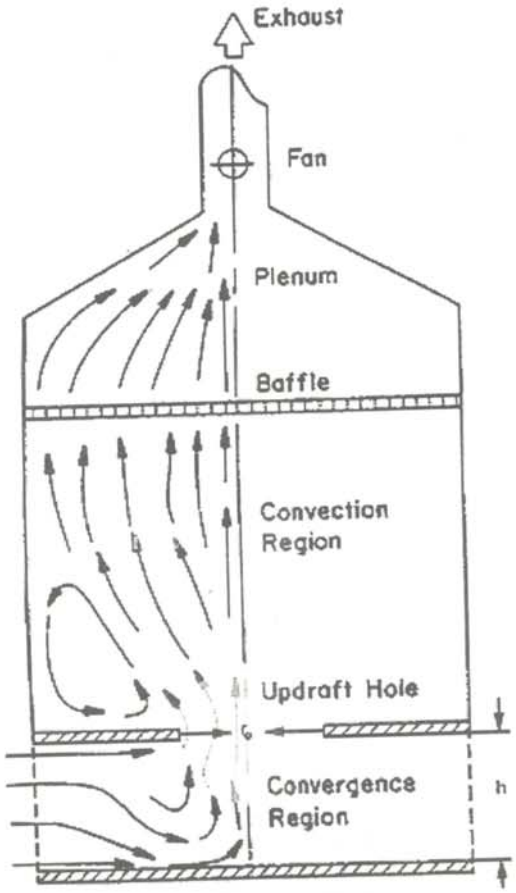

Figure 2
Schematic layout of a Ward type Tornado Vortex Chamber (TVC). The arrows mark the direction of the air flow.

laboratory have made notable progress, but the instrumentation used to probe the vortex axis was often obtrusive, and/or offered poor spatial resolution.

Due to the significant down scaling in vortex size necessary in laboratory modeling, most simulated vortex research provide highly general results, analyzing large flow fields rather than internal core dynamics. Improving the spatial resolution of airflow measurements to uncover the complex inner structure of a tornado is the driving force behind the research at the Miami TVC. Since velocity gradients in the core region are large over very small length scales, and the axis of a vortex does not maintain a completely static position with respect to the ground, the core structure is experimentally elusive.

MIAMI TVC AND RECENT IMPROVEMENTS

The best apparatus [2] for modeling tornadoes in a laboratory was the TVC designed by N.B. Ward. [3]. Ward type TVCs have been constructed at Purdue University, University of Oklahoma, Kyoto University and Miami University. The basic concept of the TVC is to provide initial vorticity and subsequent circulation to a radial inflow that converge and ascend due to an exhaust fan mounted on top of the chamber. A cylindrical baffle is placed above the convection region to straighten and scale the size of the vortex. Figure 2 shows a cross-sectional view of a Ward type TVC. A more complete discussion of Ward type TVCs and their variants can be found elsewhere. [1]

The first Ward type chambers used rotating mesh screens to provide the initial vorticity and circulation. In later chambers, the screens were replaced by arrays of steel vanes of specific chord and curvature that guided the radial inflow into a circulatory pattern. The vane method was very successful, and has since been the standard in TVC design. An important quantity in the Ward type TVC is the swirl ratio, S: the ratio of the tangential velocity, v_t, at the edge of the updraft radius to the mean vertical velocity through the updraft hole, w_o. In TVCs that uses vanes, S is defined as:

$$S = \frac{\tan(\theta)}{2a}, \tag{1}$$

where θ is the angle of inflow with respect to the radial and a is the aspect ratio defined as:

$$a = \frac{h}{r_o}, \tag{2}$$

where h is the inflow depth and r_o is the updraft radius. The swirl ratio dictates much of the vortex dynamics and morphology, and thus is usually varied often in simulated tornado research.

To change swirl ratios in a TVC using vanes, the metal plates have to be added or removed according to chord and curvature. This becomes a tedious process, and gives the researcher relatively limited control over swirl. A system of fans, as shown in Figure 3, feeding into vane-guided discharge columns installed in regular intervals around the perimeter of convergence region in the Miami TVC has

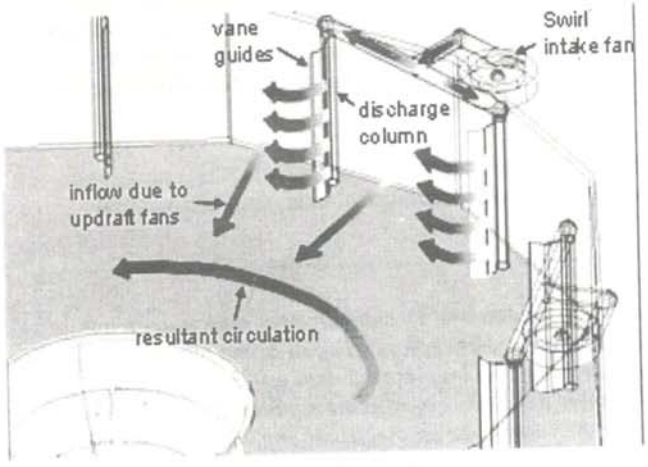

Figure 3
Overhead view of the discharge/vane-guide system. The shaded region is the chamber floor. The arrows mark the direction of the flow of the air.

improved the control over swirl. An array of six fans provide air flow to twelve discharge columns whose four-inch-chord vane-guides smooth the convergence of radial flow caused by the exhaust fans and the tangential flow of the discharge columns.

For most experiments conducted in a TVC, a vortex with static axial position is ideal. The vane-guide configuration provides less vortex wander (the random motions of the axial position of the vortex about the chamber floor due to turbulence in the convergence region) than the discharge columns alone. The fan/discharge column system does not seem to compromise any vortex position stability when compared to previous vane configurations. Using the discharge column system, the swirl in the Miami TVC can be changed by manipulating the output of a regulated power source wired in parallel with the system fan array. The swirl is then given by a combination of Equation 1, the swirl due to the vanes, and the swirl created by the discharge columns.

The height of vortex breakdown (VBD) and swirl are related. As the swirl is increased, the VBD descends to the chamber floor. This relationship is direct and fairly linear, so the swirl created by the new vane-guided discharge column system could be calibrated by comparing VBD heights in previous data sets with VBD heights in the modified chamber. [4,5]

In addition to the physical improvements to the TVC , an entirely new data acquisition system was installed. Hot-film probes in conjunction with a constant-temperature anemometer have been the most accurate and affordable way to probe the flow velocities in a simulated vortex. These small, unobtrusive probes could capture a quasi-instantaneous "snapshot" of axial or tangential flow velocities by sweeping through the vortex core. [5]

Highly crucial to the validity of these snapshots is how many times per second the output of the anemometer is sampled. Since the dimensions of the vortices studied are so small, the distance the probe travels between samples must be significantly smaller to provide accurate spatial resolution. To do this, either the sampling rate must increase, or the speed at which the probe sweeps must decrease. Since decreasing the probe sweep speed would reduce the chance of a clean swipe through the core region due to vortex wander, a system that would greatly increase the sampling rate was installed.

A high speed data acquisition board [6] was installed to take data from the constant temperature anemometer and transfer it to a personal computer via software written in LabVIEW™ specialized for the Miami TVC. This setup allowed sampling rates of over 2000 per second to be achieved, exceeding the sampling rates used in earlier hot film work by several orders of magnitude. All data reported in this research were obtained at a sampling speed of 1000 samples per second, providing spatial resolution of about 125 samples per centimeter.

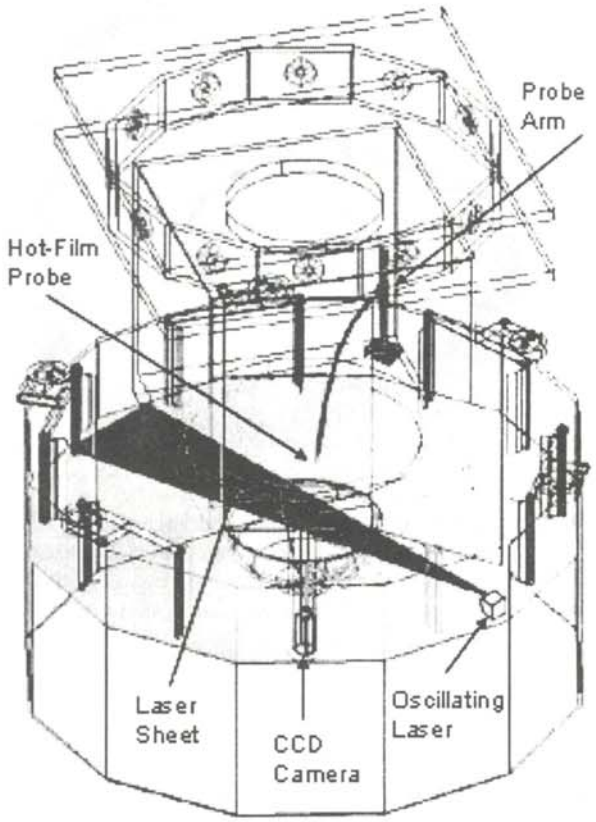

Figure 4
Overhead diagram of the vortex probing system in the Miami TVC. The light gray area is the chamber floor. The laser sheet is shown in a darker gray.

EXPERIMENTAL PROCEDURE

The velocity measurements made by hot-film probe/ constant temperature anemometer systems in this study were preceded by an extensive calibration process of all apparatus used to ensure an unprecedented level of accuracy. Each probe used was calibrated in a low flow wind tunnel in which stable flow velocities could be produced by applying a range of voltages to the tunnel fan motor. Tunnel flow velocity as a function of applied fan motor voltage was calibrated previously [5,7] However significant renovation of the wind tunnel was undertaken in preparation for this research, so recalibration was necessary.

The most accurate way to calibrate the low flow tunnel was to insert a Pitot-static tube into the mid-tunnel flow measure a differential pressure between atmospheric pressure and the pressure deficit created by the flow through the tunnel. The pressure difference was converted to a proportional voltage using a wet-wet differential pressure transducer, which in turn was calibrated with a micromanometer.[8] The differential pressure Δp, was converted to a velocity, v, using an expression derived

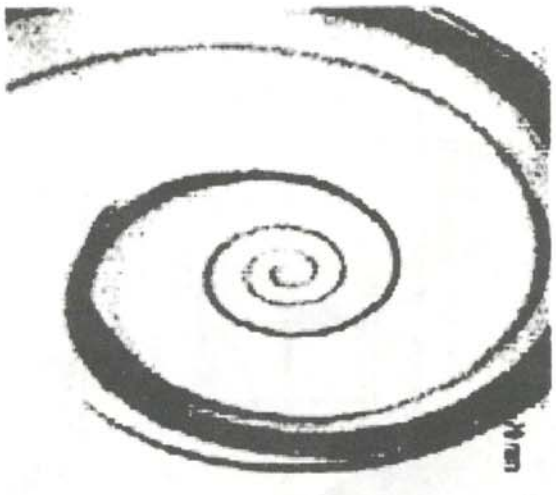

Figure 5
Digital display frame from CCD camera mounted in the TVC's crawl space. A laser sheet is created to illuminate smoke within the chamber and create a white to black contrast ratio. Colors in this picture have been inverted (black regions contain smoke).

from Bernoulli's equation:

$$\Delta p = \frac{1}{2} \rho v^2, \qquad (3)$$

where ρ is the density of air.

Of the four principle TVC parameters (swirl ratio, volume flow rate, probe height, and updraft hole radius), only swirl ratio and probe height were varied during the course of this research. The updraft hole radius was fixed at 0.255 meters and the volume flow rate through the hole was set at 0.386 m^3s^{-1}. A larger updraft radius has the advantage of creating a larger vortex cores. However, the smaller updraft hole has the benefit of reducing vortex wander. Calibration of the hot film probes showed large error bars at low wind speeds (below 1 m/s), so the volume flow rate in the TVC was selected so the average velocity through the updraft hole was about 2 m/s. This assured all wind speeds measured would be within the most accurate

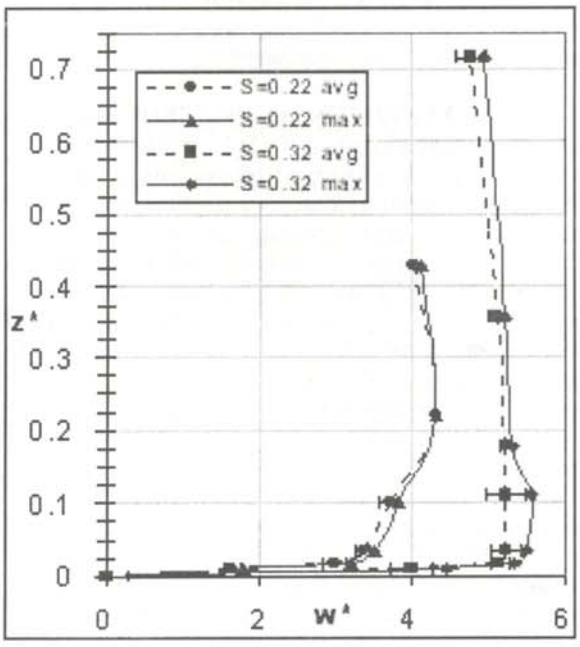

(a)

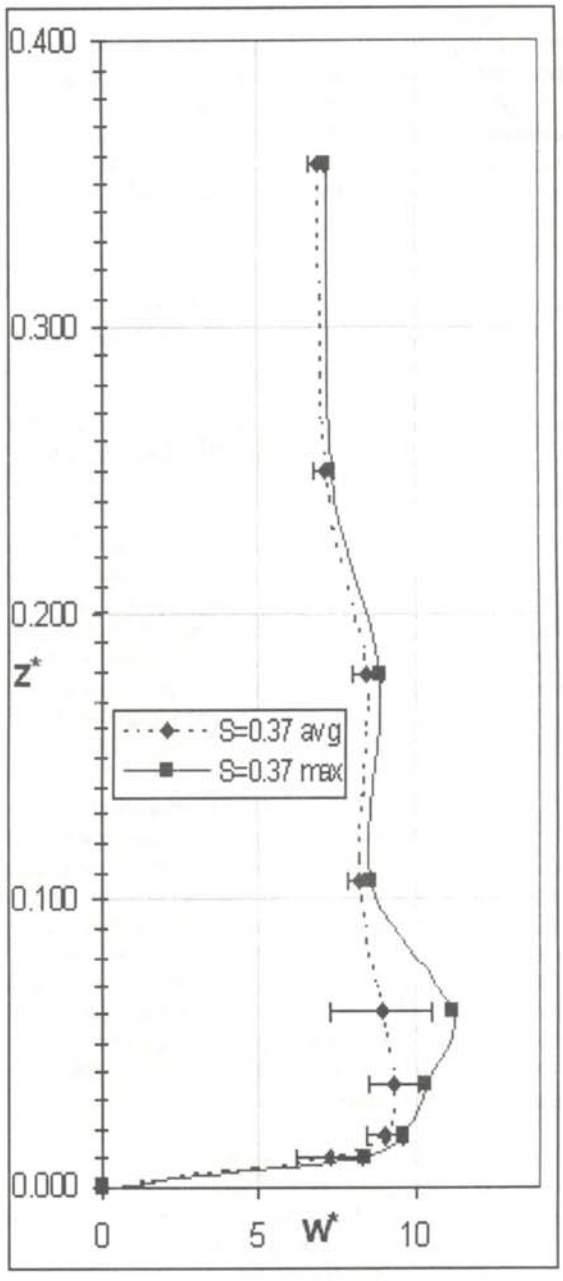

(b)

Figure 6
Axial vertical velocity profile of vortices created with swirl ratio of : (a) S=0.22 and S=0.32. (b) S = 0.37. The diamond shaped points are average values and the triangular points are maximum values

region of probe calibration.

The hot film probe was attached to a variable height, rotating mounting arm shown in Figure 4. The rotating mechanism was attached above the updraft radius. The mounting arm descends at a 45-degree angle into the convergence region, sweeping out a 15 cm arc through the vertical axis of the chamber. If the axial position of the vortex with respect to the chamber floor does not change, the 15 cm arc would always intersect the core region,

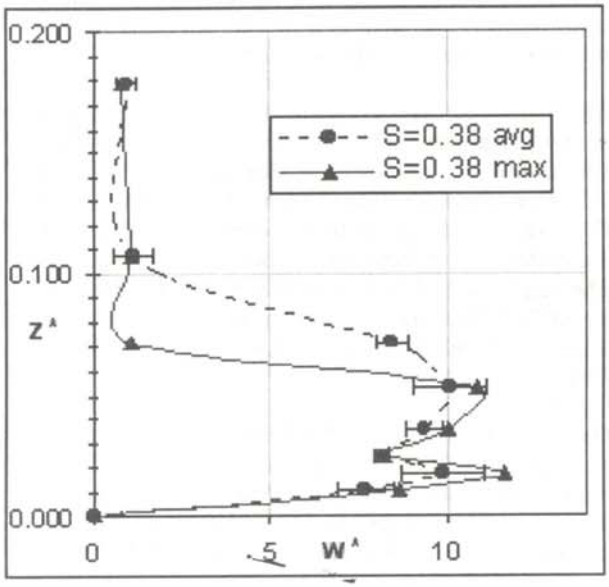

(c)

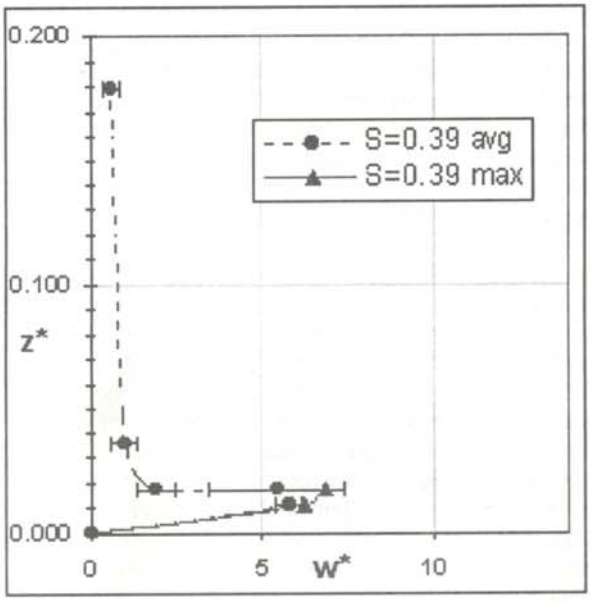

(d)

Figure 6
Axial vertical velocity profile of vortices created with swirl ratio of (c) S=0.38 and (d) = 0.39. The diamond shaped points are average values and the triangular points are maximum values

requiring only one sweep of the probe arm to obtain a vertical velocity snapshot. However, due to vortex wander, many sweeps are usually necessary to obtain just a few accurate vertical velocity snapshots.

To determine which of the sweeps actually trace the hot-film probe across a diameter of the vortex core, a digital video system was installed to monitor the axial motion of the vortex. A CCD camera mounted in the crawl space beneath the TVC floor can be focused on variable heights along the axis of the convection region through a glass aperture. For visualization purposes, smoke is introduced through the chamber floor. A small diode laser apparatus mounted near the perimeter of the convergence region can be aimed at different heights across the center of the TVC floor. The laser beam apparatus oscillates the horizontal position of the laser beam parallel to the chamber floor at roughly 60 Hz creating the effect of a "laser sheet" (see Figure 4). This thin illuminated surface highlights the smoke particles in a cross-section of the vortex core, providing a nearly white to black contrast ratio between the vortex and background, maximizing the effectiveness of video analysis. Figure 5 is an example of the video analysis. By adjusting the laser sheet to shine across the same cross-sectional plane as the probe is sweeping, visual confirmation of the path of the probe through the vortex core can be obtained.

All data taken during this research is catalogued with digital video recordings of the vortex-probe interaction. This enables each data set to be reviewed on digital slow motion and frame-by-frame video, to determine if the probe actually did make a clean sweep though the core region. In a given data acquisition run of fifteen core sweeps, only two to four sweeps were reliable data.

This data acquisition process was repeated at different probe heights for super-critical vortex flows of varying swirl ratios. For each probe height at each swirl ratio, roughly 100 sweeps through the core region were attempted and analyzed. This experimental procedure, coupled with the increased acquisition rates, allow the data from this research to presented with a level of confidence that has not been matched in the field of simulated vortex study.

RESULTS AND DISCUSSION

Axial vertical velocity profiles of vortices created at five different swirl ratios, 0.22, 0.32, 0.37, 0.38 and 0.39 were acquired. The results, shown in Figure 6, are presented as both average (dotted line), and maximum (solid line) non-dimensional height, z^*, versus non-dimensional axial vertical velocity, w^*. Error bars represent the standard deviation of the average non-dimensional velocity at a particular height. The non-dimensionalized height is calculated by dividing the probe height by the inflow depth, and dividing the resulting velocities by the average velocity through the updraft hole. Data in this form lend themselves to easy comparison to data taken in other

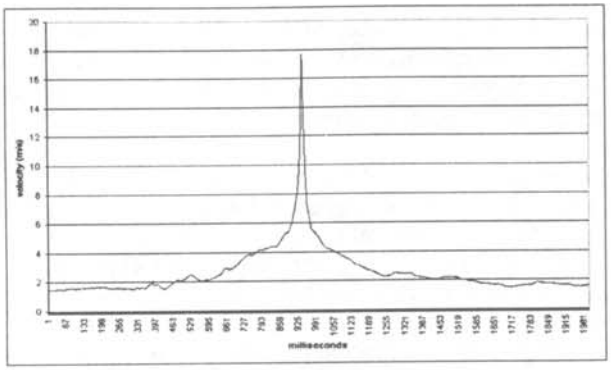

(a)

(b)

Figure 7

Example of an axial vertical velocity snapshot in (a) the super-critical region and (b) in vortex breakdown or vortex bubbling

TVCs with different physical geometries and updraft flow rates.

The super-critical region of the vortex was probed up to the height of vortex breakdown (VBD). This breakdown is a transition from a relatively smooth super-critical flow to a highly turbulent, sub-critical flow. Velocity measurements above the VBD are highly erratic and do not lend themselves to all but the most general modeling. In Figure 6(d), the steep decline of vertical velocity along the vortex axis is a signature of vortex breakdown. The maximum vertical velocities diverge from the vortex axis and trace around the surface of a bubble of nearly stagnant air. A more complete discussion of VBD structure can be found elsewhere. [1]

Axial vertical velocity snapshots taken in the vortex core appear in Figure 7. The sampling frequency of data acquisition was fixed at 1 kHz, so the core velocity could be measured once every millisecond. If the velocity of the probe arm remained constant, each sample would represent about 1 mm across the probe sweep path. Unfortunately, the probe arm travel velocity is not completely predictable. Useful spatial approximations can be made by converting the sample period to a distance. But for this research, it is more accurate to plot axial vertical velocity versus time in milliseconds as displayed in Figure 7.

The hot-film probes used are not directionally sensitive, so with the current data acquisition apparatus, the ascending walls of the spikes cannot be resolved into vertical and tangential velocity components. The maximum value of these spikes, however, represents a region of the central vortex core that is known to posses a one-dimensional vertical flow along the vortex axis. Due to the inability to resolve velocity components, interpolations of inner core radii could not be attempted with confidence. The spike width was notably less than the spike widths of data taken at the Miami TVC with smaller data sampling rates, implying greater spatial resolution.

The sharp peak seen in Figure 7(a) is characteristic of the super-critical flow. The column of rapidly ascending air is surrounded by a more slowly ascending rotating "pipe." This structure is lost during vortex breakdown, and the flow creates a double peak signature (see Figure 7(b)) with a turbulent trough between the two velocity maximums. The height of the VBD remains somewhat constant for given TVC flow and geometry arrangements and can be visually recognized through the viewing window in the TVC.

During data collection of the $S = 0.22$ and $S = 0.32$ vortices, the VBD was visually confirmed as being more than 1 meter and 0.5 meters off the chamber floor respectively, yet at low probe heights the hot-film would pick up a velocity signature that resembled that of VBD. Upon closer video analysis, it was found that the super-critical region occasionally underwent a structure breakdown, or super-critical bubbling, that would propagate up the super-critical region. This bubble would ultimately "burst" once it approached the VBD, and often significantly altered the height of the larger breakdown. The $S = 0.22$ and $S = 0.32$ data sets showed no evidence of vortex bubbling under an axial height of 20 mm, which suggests that the super critical region near the surface is more stable than the region near the VBD.

In addition to the apparent structural instability in the upper super-critical region, there was an apparent instability in axial vertical velocities in the super-critical region of high swirl vortices. The low swirl flows ($S = 0.22$ and $S = 0.32$), had very well behaved vertical velocity profiles, so much so that they could nearly be represented by an exponential or even piece-wise linear function. As the swirl was increased, the vortices' vertical axial velocities began to be less consistent at any given height. As seen in Figure 6(d), the velocity profiles begin to develop bulges near the surface and large uncertainty. The standard deviation of velocities in the core region increases markedly with increasing swirl ratio. Upon close examination of the peaks recorded at higher swirl ratios, it was realized that the physical dimensions of the inner core region were shrinking with increased swirl.

The velocities in the steep peak regions of high swirl

vortices varied by nearly a meter per second between points, implying that the actual inner core diameter was comparable to the diameter of a human hair, less than 1/125 of a centimeter. The average standard deviations of axial vertical velocities rose sharply with swirl because the inner core became increasingly more difficult to probe due to its minute size.

SUMMARY AND SUGGESTIONS FOR FURTHER RESEARCH

The precision and accuracy of the data produced in this research is probably the best that can be achieved with the hot-film/constant temperature anemometer system at the given sampling rate. Although the physical dimensions of these probes are very small, the inner core region proved to be several orders of magnitude smaller in high swirl vortices. In fact, the data obtained show that the diameter of the inner core region contracts drastically as the swirl ratio increases. Data acquisition methods that enable constant monitoring of the vortex core, such as an inproved version of laser Doppler velocimetery [9] would enhance spatial resolution. When compared to hot film sensors, laser systems are expensive, complex and , on this scale of measurement, have a relatively large sampling volume. Using higher sampling rates in a hot-film anemometer system may also provide the resolution necessary to capture peak axial vertical velocity values of high swirl super-critical vortices. The Miami TVC computer acquisition system is currently set up to take data at up to 20,000 samples per second. This research suggests that further study with film sensors in comparable sized vortices employing sampling frequencies of 2000 samples per second and above should be done. Sacrificing vortex stability by using a larger updraft hole would increase the size of the vortex core and could improve the spatial resolution.

In tornados, axial vertical velocity, in principle is the most straight forward measurement because of its one-dimensional nature. This is not the case even a fraction of a millimeter off the axis of the vortex, where the tangential component of the velocity rapidly becomes significant. For off-axis measurements, more than one sensor used simultaneously is needed to resolve vertical and tangential velocity components. A new probe arm that accommodates two mutually perpendicular hot film sensors is needed to resolve the two components of velocity. Such device would reveal much more about the core dynamics and structure as well as a more accurate determination of the core radius.

ACKNOWLEDGMENTS

The author would like to thank the Miami University OAST and the Undergraduate Summer Scholars Program for providing grant support. He acknowledges Dr. Christopher Church for providing all the apparatus and overseeing the research. Dr. Michael Pechan and Lynn Johnson provided technical expertise in implementing the data acquisition system. He acknowledges the collaboration of Karen Kosiba in the calibration process, the data acquisition and analysis.

REFERENCES

* Rota Skipper, Corp. 130 East 168th Street, South Holland, IL 60473. Clelanjd@hotmail.com

1. A good overview of the results of professional researchers studying simulated vortices can be found in The Tornado, Its Structure, Dynamics, Prediction and Hazards, American Geophysical Union, Washington, DC, (1993), pp. 277-319.
2. R.P. Davies-Jones, Proceedings from the Symposium on Tornadoes, (1976), pp. 151-173.
3. N.B. Ward, Journal of Atmospheric Sciences, 29, (1972), pp. 1194-1204.
4. J.D. Cleland, unpublished data from the MUTVC with vane configuration, (1999).
5. R.B. Carver, Master's Thesis, Department of Physics, Miami University (1993).
6. National Instruments PCI-MIO-16XE-50 Data Acquisition board.
7. C.M. Tucker, Master's Thesis, Department of Physics, Miami University ((1998).
8. A model DP103 wet-wet differential pressure transducer manufactured by Validyne.
9. D.E. Lund and J.T. Snow, The Tornado, Its Structure, Dynamics, Prediction and Hazards, American Geophysical Union, Washington, DC, (1993), pp. 297-306.

FACULTY SPONSOR

Dr. Christopher R. Church
Department of Physics
Miami University
Oxford, OH 45056-1866

FAR-INFRARED FREQUENCY MEASUREMENTS USING THE THREE-LASER HETERODYNE TECHNIQUE

Heidi Hockel * and Mike Lauters †
Department of Physics
University of Wisconsin–La Crosse
La Crosse, WI 54601
Received January 10, 2001

ABSTRACT

An optically pumped molecular laser system has been used to generate short wavelength laser emissions in the far-infrared (FIR) region. In this experiment, a 1.5 m long carbon dioxide (CO_2) laser was used to optically pump a 2 m long FIR cavity containing the methanol isotope CD_3OH. The FIR laser utilizes an X-V pumping geometry, recently shown to efficiently pump short wavelength emissions below 100 μm. Using the three-laser heterodyne technique, the frequencies of four distinct laser emissions, ranging between 67 μm and 105 μm, have been measured and are reported with a fractional uncertainty of $\pm 2 \times 10^{-7}$, permitting spectroscopic assignment of the laser transition.

INTRODUCTION

A significant part of our understanding of the physical world is through the application of measurement techniques. With the invention of the LASER (Light Amplification by Stimulated Emission of Radiation) in the 1960's, and developments in detector technology, the far-infrared region (FIR), ranging from approximately 10 μm to 1000 μm, has emerged as a viable area of study. Investigations of the FIR region with this coherent source of radiation were first performed with the electrical discharge laser. This type of laser is capable of producing approximately 340 emissions, including several very important lines from HCN, DCN, and H_2O vapor. In 1970, a pulsed emission from methyl fluoride (CH_3F) pumped by a CO_2 laser constituted the first optically pumped FIR laser. The optically pumped molecular laser (OPML) utilizes the superposition of infrared laser emissions with the absorption spectrum of the optical cavity's lasing medium. This technique quickly overshadowed the direct discharge laser because of the immense number of laser emissions it was capable of producing. Currently, there are over 5000 known OPML emissions in the FIR region.

Heidi and Mike graduated with B.S. degrees in physics from the University of Wisconsin-La Crosse. This research was performed during the summer of their junior year, when the worked with scientists at the National Institute of Standards and Technology in Boulder, CO, sponsored in part by NSF and WSGC/ NASA. Heidi is currently pursuing her Ph.D. in optics at the School of Optics/CREOL, University of Central Florida. Mike is currently pursuing his Ph.D. in optics at the Optical sciences Center, University of Arizona.

Following the initial observation of FIR laser emissions from methanol (CH_3OH) [1], methanol and its isotopes have produced more than 2000 FIR laser lines in the wavelength range 21.7 μm – 3030.0 μm, with CD_3OH contributing over 400 emissions alone. [2-4] The richness of FIR emissions is principally due to the excellent overlap between the CD_3-deformation region (1068.2 cm^{-1}) and the C-O vibrational band (984.4 cm^{-1}) with the 9 μm and 10 μm CO_2 laser bands, respectively. [5, 6] This overlap, combined with the torsional motion exhibited by CD_3OH, makes this molecule a prolific source of FIR laser emissions.

In this paper, we discuss the experimental setup of the OPML and three-laser heterodyne systems and report the measured frequencies of the optically pumped FIR laser emissions from CD_3OH. The coherence of the continuous-wave laser's radiation is most accurately measured using direct frequency measurements, which do not suffer from the limitations of wavelength measurements.

THE EXPERIMENT

CO_2 Laser System

There are three necessary components to any laser system: an optical cavity, a pumping mechanism, and a lasing medium. The CO_2 pump laser, shown in Fig. 1, is 1.5 m long and includes a partially ribbed cavity surrounded by a water-cooled jacket. The pumping mechanism is in the form of a 13,000 V power supply capable of providing 50 mA to each cathode. The laser medium is a flowing gas

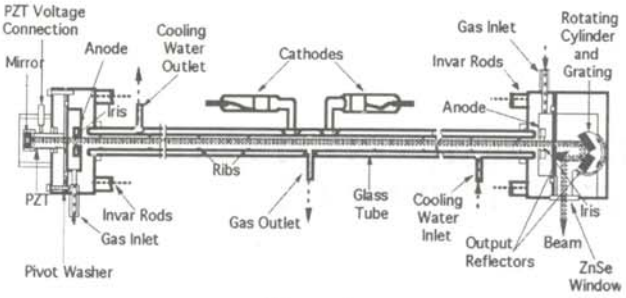

Figure 1
Top view of the CO_2 laser.

mixture of CO_2, nitrogen, and helium in the ratio 1:1.2:7.8 with CO_2 producing the laser emissions while helium and nitrogen act as buffer gases. The Pyrex glass tube has an inner diameter of 18 mm and contains five equally spaced glass ribs whose inner diameters increase from 16.5 to 17.5 mm. By introducing glass ribs into the laser cavity, many wall bounce modes are eliminated, thereby forcing an open structure mode and increasing the effective resolution of the grating. [7] The laser uses the zeroth-order output coupling from a 133 line/mm grating with 3% output coupling in zero order. A high-reflectivity gold-coated 20-m radius-of-curvature mirror, attached to a piezo-electric transducer (PZT), is used on the other end. The PZT permits the fine adjustment of the end mirror, allowing the CO_2 laser radiation to be kept tuned to its center frequency.

The CO_2 laser is capable of producing approximately 275 lines, including emissions from the 'regular', 'hot', and sequence bands. These bands indicate the vibrational levels responsible for laser action. The vibrational transitions in question are centered at 9.5 μm and 10.4 μm for the regular band, 9.3 μm and 10.8 μm for the hot band, 9.43 μm and 10.4 μm for the sequence band. [4] Within each of these vibrational transitions are two allowed possibilities for the change in the rotational quantum number, J, namely $\Delta J = J_{upper} - J_{lower} = -1$ (P-branch) or $\Delta J = +1$ (R-branch). Conventionally, a transition is designated by (for example) 10P(34), indicating the 10 μm regular band P-branch transition from the $J_{upper} = 33$ to the $J_{lower} = 34$ level. [10HP(34) would indicate a hot-band emission while 10SP(34) would indicate a sequence-band emission.] Both the 9 μm and 10 μm branches exhibit laser emission out of 9R(58), 9P(60), 10R(58) and 10P(60) with powers up to 30 W for the regular laser lines and 10 W for the hot-band and sequence-band emissions.[8]

OPML System

The experimental setup for the OPML system is partially shown in Fig. 2. The CO_2 laser radiation is focused into the FIR cavity with a 12 m radius-of-curvature gold coated concave mirror, externally mounted on the far (fixed mirror) end of the cavity at approximately 2 m from the 20 mm diameter ZnSe window. A flat gold coated mirror then reflects the CO_2 beam into the FIR cavity and to the X-V mirror system. This mirror system, shown in Fig. 2, uses three 19-mm diameter copper mirrors along with one of the FIR cavity mirrors. Each of the four copper mirrors extend about 20 mm into the FIR cavity and transmit approximately 99% of the 118.8 μm line of CH_3OH through the FIR window. (The 118.8 μm line of CH_3OH is the strongest known optically pumped FIR laser emission.) The advantage to this is that many of the longer wavelength lines are suppressed, thereby allowing some of the shorter wavelengths to emerge.

In the pumping geometry, shown in Fig. 2, a 45° mirror first reflects the beam across the vertical plane of the cavity (path 1). At the other end, two identical 45° mirrors are used to redirect the CO_2 beam to the bottom of the input chamber (paths 2 and 3 which complete the X-portion of the pumping scheme). A gold-plated copper mirror with a 1 m radius of curvature then reflects the CO_2 beam to the main FIR cavity mirror (path 4). This curvature was chosen so that the beam diameter would be slightly larger than a 40 μm Gaussian beam waist. This optimizes the overlap between the CO_2 laser beam and the short wavelength FIR emissions. Finally the CO_2 beam is reflected from the FIR mirror, to the input 45° mirror, and out of the FIR system (path 5 which completes the V-portion of the pumping scheme). One advantage to this type of pumping design over simpler configurations, such as the V-pumping geometry, is that the additional passes allow more of the gain medium to be pumped.

The FIR cavity is about 2 m long and utilizes a nearly confocal mirror system, consisting of two 1.9 m radius-of-curvature concave gold-coated copper mirrors with a 50 mm diameter. Four Invar rods connect the end plates holding the FIR mirrors and the 2 m long, 59 mm inner diameter, Pyrex glass tube. One copper mirror is attached to a micrometer and is moved to tune the FIR cavity. The output coupling is varied by moving the 45° copper mirror radially in and out of the cavity mode. The generated FIR radiation is then sent through a polypropylene window, 0.634 μm thick, and focused by an off-axis parabolic mirror onto a metal-insulator-metal (MIM) point contact diode.

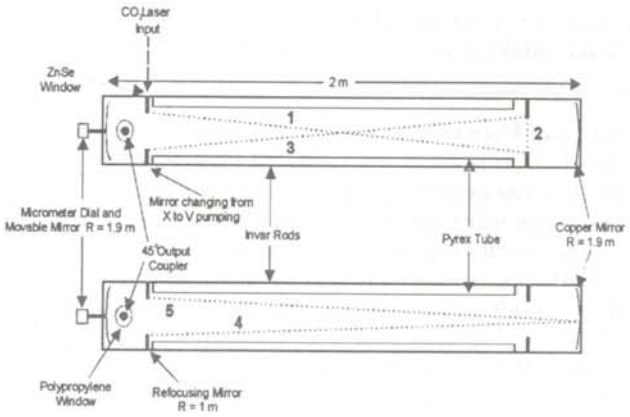

Figure 2
Side view of the optically pumped molecular laser system.

Wavelength measurements

Initial wavelength measurements of the FIR radiation were made by tuning the Fabry-Perot cavity with the movable end mirror and measuring the mirror displacement for 20 wavelengths of that laser mode. The value obtained is accurate to within ± 0.5 μm. A set of absorbing filters, calibrated by wavelength, discriminates against CO_2 laser radiation reaching the detector as well as helping distinguish different FIR wavelengths. The relative polarizations of the FIR emissions with respect to the CO_2 laser lines were measured with a multi-Brewster-angle polarization selector.

Frequency Measurements

FIR laser frequencies were measured using the three-laser heterodyne technique discussed elsewhere. [9,10] In general, different but known frequencies are mixed together to produce a sum or difference frequency. This frequency is then combined with a signal of unknown frequency. A "beat", analogous to the beat heard between two musical tones, between the unknown and the sum or difference frequency can then be observed on a spectrum analyzer. If the separation between these frequencies is greater than the range of the spectrum analyzer, a microwave source may be added to decrease the gap.

The experimental setup is shown in Fig. 3. Two CO_2 laser frequencies were combined to create a difference frequency in the FIR region. The particular lines chosen to generate the difference frequency were based on the wavelength measurement of the unknown FIR emission. These CO_2 frequencies were stabilized by locking each laser to a saturation dip in the 4.3 μm fluorescence signal from an external reference cell.

The beat note, monitored by means of a spectrum analyzer, shown in Fig. 4, is used to determine the unknown frequency ν_x through the relation:

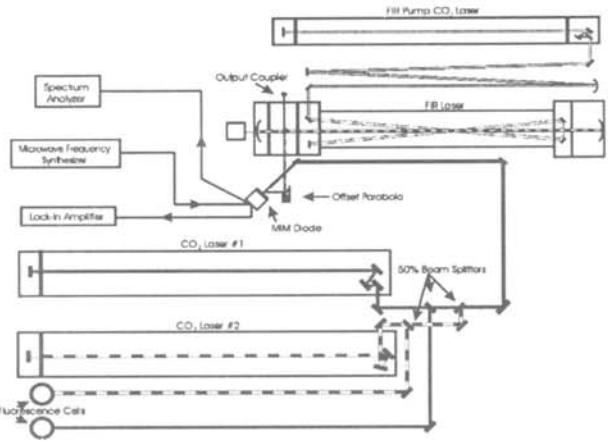

Figure 3

Diagram of the FIR laser and the frequency measurement setup.

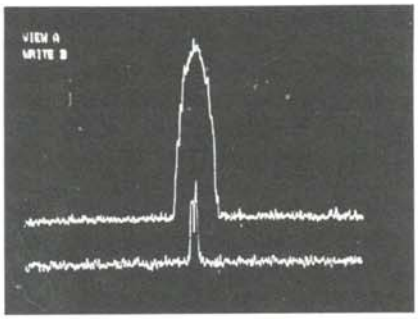

Figure 4

Spectrum analyzer display of the time-averaged beat note between the difference frequency (generated by the 9R(18) and 10R(30) CO_2 laser lines), the microwave source and the unknown FIR frequency. The center frequency is 2 850 703.9 MHz.

$$\nu_x = n_1 \nu_{CO2} \pm n_2 \nu_{\mu w} \pm \nu_{beat}, \quad (1)$$

where ν_{CO2} is the difference frequency synthesized by two CO_2 lasers, $\nu_{\mu w}$ the microwave frequency, and ν_{beat} the beat frequency. The integers, n_1 and n_2, define the mixing order of the difference and microwave frequencies, respectively (first-order, second-order, etc.).

A MIM point contact diode was used as a harmonic mixer, combining the signals from the laser and microwave sources. The signal from the MIM diode was fed into a preamplifier connected to a spectrum analyzer [11] to measure the intermediate frequency beat note by comparison with a marker generated by a synthesizer [11]. When necessary, a microwave source[11], operating between 0 and 18 GHz was used. The values of n_1 and n_2, as well as the ± sign in Equation 1 are determined experimentally by either tuning the FIR laser cavity or by increasing (or decreasing) the microwave frequency slightly to get a small shift in the beat note on the spectrum analyzer.

The one-sigma uncertainty of frequency measurements is $\Delta\nu/\nu = 2 \times 10^{-7}$. It is due mainly to the uncertainty in the setting of the FIR laser cavity to the center of its gain curve. For minimizing this uncertainty, we tuned the FIR laser across its gain curve and observed the change to the beat note on the spectrum analyzer using a peak hold feature. The value of this frequency is calculated from the average of ten measurements recorded with varying microwave frequencies. In addition, these measurements were made with at least two different sets of CO_2 laser lines.

DATA PRESENTATION AND INTERPRETATION OF RESULTS

In Table 1, we show the five new frequencies measured, arranged in order by their pump lines. The wavelengths and wavenumbers were calculated from the average frequency using 1 cm^{-1} = 29 979.2458 MHz. All FIR emissions were observed to have parallel (||) polarizations with respect to the CO_2 laser. With the laser emission from the 10R(32) pump line, two peaks were observed.

CO_2 Pump	Frequency (MHz)	Wavelength (μm)	Wavenumber (cm^{-1})
9R(6)	4 413 279.1	67.930	147.2111
10R(32)	3 582 585.2	83.680	119.5022
10R(32)	3 582 579.9	83.680	119.5020
10R(16)	3 463 216.2	86.565	115.5205
10P(32)	2 850 703.9	105.164	95.0892

Table 1

New frequencies measured for the laser emissions from optically pumped CD_3OH. All FIR emissions have their polarization parallel to those of the CO_2 pump lines.

These peaks, separated by approximately 5.3 MHz, may indicate a doublet or an experimental artifact based on the laser cavity used. This includes, but is not limited to, the possibility of observing a higher order TEM mode, or by pumping the FIR medium on the edge rather than in the center of its gain curve. The existence of a doublet only can be proven by determining its spectroscopic assignment. Experimental verification could be found by observing this line in another type of FIR cavity. The FIR frequencies were measured for the first time in this work under optimal operating conditions. A slight shift in frequency (possibly a few MHz) may still occur due to the type of FIR cavity and pumping geometry used. [8, 12, 13]

The expansion of frequency measurement techniques from the microwave to the optical regions has made a significant impact on the fields of metrology and spectroscopy. Despite the uncertainties, the FIR frequencies measured here represent an increase in accuracy over the calculated frequencies for CD_3OH. The frequencies measured using this OPML system, with the X-V pumping geometry, will be useful for future assignments of FIR laser emissions from this molecule by calculation of combination loops from high-resolution Fourier transform data. [14] These results can also be used for laser Stark and laser magnetic resonance spectroscopy where OPML emissions serve as a source of strong coherent FIR radiation. Finally, the information gained from these frequencies will help provide a more complete picture of CD_3OH in the far-infrared region.

ACKNOWLEDGMENTS

The authors wish to acknowledge the following programs for financial support: the National Science Foundation (CRIF - #9982001 and RUI - #0078812), the Wisconsin Space Grant Consortium (Research Seed Grant and Undergraduate Research Award), the College of Science and Allied Health (Faculty Research Grant and Undergraduate Research Grant), and the University of Wisconsin-La Crosse Undergraduate Research Grant.

REFERENCES

* Current address of author: School of Optics/Center for Research and Education in Optics and Lasers, University of Central Florida, Orlando, FL 32816-2700.

† Current address of author: Optical Sciences Center, University of Arizona, 1630 e. University Blvd., Tuscon, AZ 85721.

1. T. Y. Chang, T. J. Bridges and E. G. Burkhard: Appl. Phys. Lett., 17, (1970), p. 249.
2. S. C. Zerbetto and E. C. C. Vasconcellos: Int. J. Infrared Millimeter Waves, 15, (1994), p. 889.
3. D. Pereira, J. C. S. Moraes, E. M. Telles, A. Scalabrin, F. Strumia, A. Moretti, G. Carelli and C. A. Massa: Int. J. Infrared Millimeter Waves, 15, (1994), p. 1.
4. N. G. Douglas, Millimetre and Submillimetre Wavelength Lasers: A Handbook of CW Measurements, (Springer-Verlag), 1989.
5. I. Mukhopadhyay, M. Mollabashi and R. M. Lees: J. Opt. Soc. Am. B., 14, (1997), p. 2227.
6. F. C. Cruz, A. Scalabrin, D. Pereira, P. A. M. Vazquez, Y. Hase and F. Strumia: J. Mol. Spectrosc., 156, (1992), p. 22.
7. E. C. C. Vasconcellos, S. C. Zerbetto, J. C. Holecek and K. M. Evenson: Opt. Letts., 20, (1995), p. 1392.
8. E. M. Telles, H. Odashima, L. R. Zink and K. M. Evenson: J. Mol. Spectrosc., 195, (1999), p. 360.
9. M. Inguscio, N. Ioli, A. Moretti, F. Strumia and F. D'Amato: Appl. Phys. B., 40, (1986), p. 165.
10. F. R. Petersen, K. M. Evenson, D. A. Jennings, J. S. Wells, K. Goto and T. J. Bridges: IEEE J. Quantum Electron., 11, (1975), p. 838.
11. We used a HP8558B spectrum analyzer; a HP8640B synthesizer; a HP8672A sweeper; all manufactured by Hewlett Packard. The product information is given for technical reference only, and does not constitute an endorsement of the equipment used in the experiment.
12. E. M. Telles, L. R. Zink and K. M. Evenson: J. Mol. Spectrosc., 191, (1998), p. 206.
13. M. Inguscio, L. R. Zink, K. M. Evenson and D. A. Jennings: IEEE J. Quantum Electron., 26, (1990), p. 575.
14. G. Moruzzi, B. P. Winnewisser, M. Winnewisser, I. Mukhopadhyay and F. Strumia, Microwave, Infrared, and Laser Transitions of Methanol: Atlas of Assigned Lines from 0 to 1258 cm^{-1}, (CRC Press, Inc.), 1995.

FACULTY SPONSORS

Dr. Michael Jackson
Rm. 2005 Cowley Hall
Department of Physics
University of Wisconsin–La Crosse
La Crosse, WI 54601
jackson.mic2@uwlax.edu

Dr. Michael D. Allen and Dr. Kenneth M. Evenson
Time and Frequency Division, 847.00
National Institute of Standards and Technology
325 Broadway
Boulder, CO 80303
mallen@boulder.nist.gov
evenson@boulder.nist.gov

PREPARING A MANUSCRIPT FOR PUBLICATION

Rexford E. Adelberger, Editor

Perhaps the most important thing for you to keep in mind when you write a manuscript which you intend to submit for publication to the Journal of Undergraduate Research in Physics is that the audience that will be reading the paper is junior or senior physics majors. They are knowledgeable about physics, but unlike you, they have not spent as much time trying to understand the specific work which is being reported in your paper. They also can read English well, and expect the paper to be written by a colleague, not a robot or an 'all-knowing' computer. There is a big difference between the comments you write in the margin of your lab notebook or what you might write in a technical brief and what you should present in a paper for publication in a scientific journal.

There is a significant difference between a Journal article and keeping a journal. Your laboratory data book should be the journal of what you did. It contains all the data, what you did (even if it was an attempt that turned out to be wrong), as well as comments as to what you were thinking at that time. The Journal article is an discussion of how you would do the research without excursions along blind alleys and hours spent collecting data that were not consistent. The reader does not have to be able to completely reproduce the work from the Journal article. The reader should be able to understand the physics and techniques of what was done.

How a person uses Journal articles to find out about new ideas in physics is often done in the following way. A computerized search, using key words in abstracts, is performed to find what work others have done in the area of interest. If the abstract seems to be about the question of interest, the body of the paper is tracked down and read. If the reader then wants to find out the finer details of how to reproduce the experiment or the derivation of some equation, the author of the paper is contacted for a personal in-depth conversation about the more subtle details.

The general style of writing that should be followed when preparing a manuscript for publication in the Journal is different from what you would submit to your English literature professor as a critique of some other work. The narrative of the paper is intended to do three things: 1) present the background necessary for the reader to appreciate and understand the physics being reported in the paper; 2) discuss the details of what you did and the implications of your work; 3) lead the reader through the work in such a way that they must come to the same concluding points that you did. When finished with your paper, the reader should not have to go back and try to decide for themselves what you did. Your narrative should lead them through your work in an unambiguous manner, telling them what to see and understand in what you did. The interpretation of the data or calculations should be done by the writer, not the reader. The interpretation of your results is the most important part of the paper.

You should take care to make sure that the material is presented in a concise logical way. You should make sure that your sentences do not have too many dependent clauses. Overly complicated sentences make the logic of an argument difficult to follow. You should choose a paragraph structure that focuses the attention of the reader on the development of the ideas.

A format which often achieves these aims is suggested below:

ABSTRACT : An abstract is a self contained paragraph that concisely explains what you did and presents any interesting results you found. The abstract is often published separately from the body of the paper, so you cannot assume that the reader of the abstract also has a copy of the rest of the paper. You cannot refer to figures or data that are presented in the body of the paper. Abstracts are used in computerized literature searches, so all key words that describe the paper should be included in the abstract.

INTRODUCTION: This is the section that sets the background for the important part of the paper. It is not just an abbreviated review of what you are going to discuss in detail later. This section of the narrative should present the necessary theoretical and experimental background such that a knowledgeable colleague, who might not be expert in the field, will be able to understand the data presentation and discussion. If you are going to use a particular theoretical model to extract some formation from your data, this model should be discussed in the introduction.

Where appropriate, factual information should be referenced using end-notes. When presenting background information, you can guide the reader to a detailed description of a particular item with the statement such as: *"A more detailed discussion of laminar flow can be found elsewhere [1]"*. If you know where there is a good discussion of some item, you don't have to repeat it, just guide the reader to the piece.

How one proceeds from this point depends upon whether the paper is about a theoretical study or is a report on an experiment. I will first suggest a format for papers about experimental investigations and then one that describes a theoretical derivation.

Experimental Investigations

THE EXPERIMENT: This section guides the reader through the techniques and apparatus used to generate the data. Schematic diagrams of equipment and circuits are often easier to understand than prose descriptions. A statement such as *"A diagram of the circuit used to measure the stopping potential is shown in Figure 6"* is better than a long elegant set of words. It is not necessary to describe in words what is shown in a diagram unless you feel that there is a very special part which should be pointed out to the reader. If special experimental techniques were developed as part of this work, they should be discussed here. You should separate the discussion of the equipment used to measure something from your results. This section should not include data presentations or discussions of error analysis.

DATA PRESENTATION AND INTERPRETATION OF RESULTS: This is the most important section of the paper. The data are the truths of your work. This section should lead the reader through the data and how errors were measured or assigned. The numerical data values are presented in tables and figures, each with its own number and caption, e.g.. *"The results of the conductivity measurements are shown in Table 3"*. It is difficult to follow narratives where the numerical results are included as part of the narrative. Raw, unanalyzed data should not be presented in the paper. All figures and tables should be referred to by their number. Any figure or table that is not discussed in the narrative should be eliminated. Items which are not discussed have no place in a paper.

A Theoretical Study

THE MODEL: This part should consist of a theoretical development of the constructs used to model the physical system

under investigation. Formulae should be on separate lines and numbered consecutively. The letters or symbols used in the equations should be identified in the narrative, e.g.. *The potential can be approximated as:*

$$W \approx Z - \sigma(\rho) \ , \qquad (1)$$

where Z is the number of protons and σ is the screening constant that is dependent on the charge density, ρ, of the inner electrons of the K and L shells. If you wish to use this formula at a later time in the narrative, you refer to it by its number, e.g.. "*The straight line fit shown in Figure 3 means that we can use Equation 1 to extract a value of...*"

CALCULATIONS: This section presents a summary and discussion of the numerical results calculated from the model. The results should be presented in tables or graphs, each with a caption. A table or graph that is not discussed in the narrative should be eliminated. Data that are not interpreted by the writer have no place in a paper. One should reference numerical results that are used in the calculations and come from previous work done by others .

The following sections pertain to both types of papers.

CONCLUSIONS: It is indeed rare that one can come to clear and meaningful conclusions in one paper. I do not know of many papers where this section should be included.

REFERENCES: All references, numbered in order from beginning to end of the paper, are collected together at the end of the paper. You should be aware of the following format:

If the reference is a text-

1. A.J. Smith and Q.C.S. Smythe, Electromagnetic Theory, Addison Wesley, New York, (1962), p. 168.

If the reference is a journal-

2. J. Boswain, Journal of Results, 92, (1968), pp. 122-127.

If the reference is unpublished-

3) R.J. Ralson, private communication.

ACKNOWLEDGMENTS: This short section should acknowledge the help received (that is not referenced in the previous section) from others. This is where you would give credit to a lab partner or someone in the machine shop who helped you build a piece of equipment.

OTHER ADVICE

TABLES AND FIGURES are placed by the layout editors at the corners of the page to make the format attractive and easy to read. Often a figure is not on the same page as the discussion of the figure. Each table or figure should be numbered and have a caption which explains the figure. Readers scan papers by looking at the figures and data tables before they read the narrative of the work. Take care to put enough information in the caption of a figure or table so that the reader can get some feeling for the meaning of the data presentation. All lines shown on graphs should be identified, e.g.. *"The dashed line is drawn to guide the eye"* or *"The solid line is a fit to the data using the Ising model"*

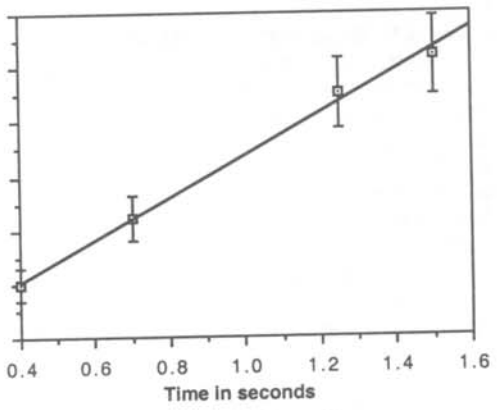

Figure 1

A graph of the measured thrust of a D-2 model rocket engine as a function of time. The line drawn is the least squares fit straight line to the data.

State	Experimental eV	Theoretical eV
3S	5.15±01	5.13
4S	1.89±02	1.93
3P	2.96±02	3.02

Table 1

Energy states found in the numerical search. The accepted values for these states are also listed.

An example of a graph of a set of data is shown in Figure 1. The graph is sized by the range of data points. The bottom left point does not have to be the point (0,0). Error bars are shown with the data points. A graph with all the data points clustered in one small corner and lots of white space does not help the reader get a feeling of the dependence of your data. Be careful that the figures you present are not too busy; too much information on a figure makes it difficult to pick out the important parts.

NUMBERS AND UNITS Any experimentally measured data presented in tables (such as shown in Table 1), should include an uncertainty. You should use scientific notation when presenting numbers, $(7.34 \pm .03) \times 10^7$ eV. Take care that you have the correct number of significant digits in your results; just because the computer prints out 6 digits does not mean that they are significant. You should use the MKS system of units.

STYLE It is often helpful to make a flow chart of your paper before you write it. In this way, you can be sure that the logical development of your presentation does not resemble two octopuses fighting, but that it is linear.

One generally writes the report in the past tense. You already did the experiment. You also should use the third person neuter case. Even though you might have done the work by yourself, you use "we". e.g.. *"We calculated the transition probability for..."* It is often confusing when you begin sentences with conjunctions. Make sure that each sentence is a clear positive statement rather than an apology.

There are a few words or phrases you should be careful of using. ***Fact*** - this is a legal word. I am not sure what it means in physics. ***Proof or prove*** - These words are meaningful in mathematics, but you can't prove something in physics, especially experimental physics. ***The purpose of this experiment is...*** Often it is necessary to do the experiment to complete the requirements for your degree. You do not need to discuss the purposes of the experiment. ***One can easily show that...*** - Don't try to intimidate the reader. What if the reader finds it difficult to show? Remember that the reader of your paper is a senior in college! ***It is obvious that... or One clearly can see....*** - Such statements only intimidate the reader that does not find your work trivial. What is obvious to someone who has spent a lot of time thinking about it may not be obvious to the reader of your paper. ***Data*** is the plural form of the noun datum. *"The data are ..."* or *"The data show that ...."*